NUMERICAL ANALYSIS OF HELICAL AND LOG-PERIODIC ANTENNAS FOR SHORT PULSE APPLICATIONS

A THESIS IN

Electrical Engineering

Presented to the Faculty of the University

of Missouri-Kansas City in partial fulfillment of

the requirements for the degree

MASTER OF SCIENCE

by

WALEED AL-SHAIKHLI

B.S., University of Missouri – Kansas City, 2018

Kansas City, Missouri

2020

NUMERICAL ANALYSIS OF HELICAL AND LOG-PERIODIC ANTENNAS FOR SHORT PULSE APPLICATIONS

Waleed K. Al-Shaikhli, Candidate for the Master of Science Degree

University of Missouri – Kansas City, 2020

ABSTRACT

The planar log-periodic (LP) and helical antennas are numerically studied as two antennas with a wide range of applications. The advantages of the LP antenna are the large adjustable bandwidth as a frequency independence radiator, its low profile, and that it can be made to be elliptically polarized. The main advantages of a helical antenna are its excellent power handling capability and tunable gain. The helical antenna is widely used in many UWB applications such as Radar, satellite communication, GPS, and other short-pulse applications. High far-field gain is essential to many applications, but a tradeoff between gain, and time-domain dispersion exists if the input of the helical antenna is to consist of short-pulses. To quantify the level of dispersion, the antennas considered in this work are modeled as linear systems, and their time-domain impulse response is calculated using CST Microwave time-domain and FEKO frequency-domain simulations of the structure. A comprehensive parametric study of the helical antenna is conducted in FEKO followed by a multigoal optimized design of an L band helical antenna to minimize pulse dispersion, size, and input impedance while maximizing far-field gain and pulse shape preservation.

APPROVAL PAGE

The faculty listed below, appointed by the Dean of the School of Computing and Engineering have examined a thesis titled “Numerical Analysis of Helical and Log-periodic Antennas for Short Pulse Applications,” presented by Waleed Al-Shaikhli, candidate for the Master of Science degree, and certify that in their opinion it is worthy of acceptance.

Supervisory Committee

Ahmed M. Hassan, Ph.D., Committee Chair

Department of Computer Science & Electrical Engineering

Deb Chatterjee, Ph.D.

Department of Computer Science & Electrical Engineering

Anthony Caruso, Ph.D.

Department of Physics and Astronomy

Mahrukh Khan, Ph.D.

Department of Computer Science & Electrical Engineering

TABLE OF CONTENTS

LIST OF ILLUSTRATIONS

FIGURE PAGE

LIST OF TABLES

TABLE PAGE

LIST OF ABBREVIATIONS

CW	Continuous Wave
EM	Electromagnetic
EMC	Electromagnetic Compatibility
FCC	Federal Communications Commission
FD	Frequency Domain
FWHM	Full Width at Half Maximum Time
GA	Genetic Algorithm
IRA	Impulse Radiating Antenna
LHS	Left-Hand Sense
LP	Log-Periodic
PCB	Printed Circuit Board
PLA	Polylactic Acid
RCS	Radar Cross Section
RF	Radio Frequency
RHS	Right-Hand Sense
TD	Time Domain
TL	Transmission Line
VSWR	Voltage Standing Wave Ratio

ACKNOWLEDGMENTS

I thank my thesis committee members Dr. Ahmed Hassan, Dr. Deb Chatterjee, Dr. Anthony Caruso, and Dr. Mahrukh Khan, for their effort to evaluate and improve this work. I am especially grateful to Dr. Hassan's mentorship that expanded my horizon as an engineer over the last few years. His passion for knowledge and work ethic are an example to follow, and I have been fortunate to be his student. This research was supported in part by the Office of Naval Research (ONR) grants: #N00014-17-1-2932 and #N00014-17-1-3016.

I am indebted to Mohamad Hamdallah, Blake Willing, and Khadimul Islam for the example they set, their encouragement, and friendship. Further, I want to thank my siblings Mohammed, Fatima, and Mayar for their constant support and the motivation they gave me to keep pushing. Finally, I want to thank my parents, Dhuha and Khalid, for their countless sacrifices, endless love, and life-long inspiration.

CHAPTER 1
ANTENNA INTRODUCTION AND DEFINITIONS

Motivation for Work

The motivation of this work is to numerically study the performance of ultrawideband antennas that provide high gain, are as small as possible, have excellent time-domain characteristics, and are capable of being incorporated into a steerable array. Some of these requirements are contradictory, such as small size vs. high boresight gain, or high gain vs. time-domain performance, satisfying all requirements is challenging if even possible. Therefore, the goal of this work is to numerically study several antenna classes to determine which class satisfies many or all the desired requirements.

The Antenna Concept

Antennas are the prime source and sensor of a wireless electromagnetic system. They function primarily to send and receive signals, as a spatial filter to direct signals in a specific direction, as an impedance transformer between the source circuit (typically 50Ω) to the impedance of the medium of propagation (typically 377Ω), and as a bandpass filter over the operating bandwidth. The IEEE Standard for Antennas defines an antenna as the part of a transmitting or receiving system designed to radiate or receive electromagnetic waves. The standard assumes an antenna is a passive, linear, and reciprocal [1]. The term passive means the antenna structure does not contain an amplifier or other active nonlinear elements such as diodes or transistors [1]. Reciprocity here implies a pulse going through a transmitting antenna sees an equivalent response to the same pulse going through a receiving antenna

[2]. An antenna in the transmit mode converts a source signal from the generator circuit to a propagating electromagnetic (EM) wave in an external medium, often air [3]. In contrast, an antenna in the receive mode converts the propagating EM wave in the external medium to an electric signal presented to the receiver's circuit.

Antenna Figures-of-Merit

Antenna performance is characterized by several parameters to describe their suitability for the application. In this section, we discuss the most common figures of merit for antenna performance.

Radiation Patterns

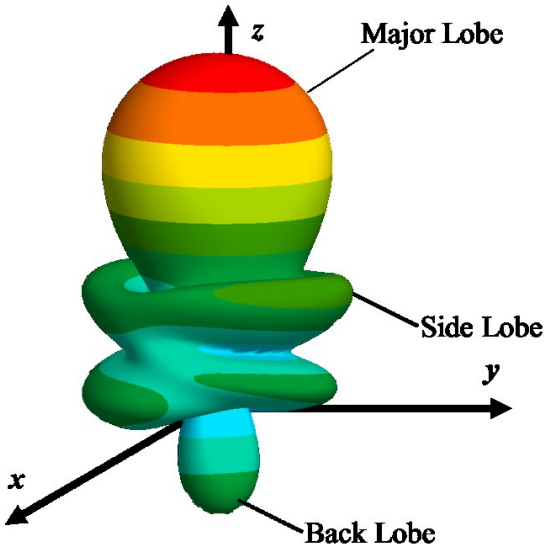

Figure 1. Antenna 2D field pattern

A radiation pattern is a mathematical description of an antenna's spatial radiation properties within a coordinate system. The radiation pattern of an antenna is determined in the far-field, and it is most commonly plotted in 2D, or 3D spherical coordinates, cartesian

and cylindrical coordinates are used less commonly. Several radiation properties can be described by radiation patterns, such as electric/magnetic field strength, gain, polarization, power flux density, or radiation intensity. Radiation patterns can be represented by a linear or dB scale. The portion of the radiation pattern bounded by angles of weaker radiation is called a lobe. The main lobe is the lobe that contains the direction of maximum antenna radiation. Other lobes can be defined for an antenna such as back lobes or sidelobes, as shown in Figure 1 [3].

Beamwidth, Directivity, and Gain

Antenna figures of merit are often referenced to an isotropic radiator, which is an ideal antenna having an equal radiation pattern in all directions [3]. An omnidirectional antenna such as the half dipole radiates power roughly equally in all directions within a plane, having a doughnut-like shape [3]. Most antennas are directional in some way, radiating more effectively in some direction more than others. This directionality of an antenna's pattern is characterized in several ways, including Beamwidth, Directivity, and Gain [3].

Beamwidth

Beamwidth is the angle of the main lobe where the antenna is radiating an identical value, typically at half of its power normalized to the max power of the lobe in any direction. There is a tradeoff between beamwidth and sidelobe levels, whereas the beamwidth decreases, the side lobe increases, and vice versa. In radar applications, the beamwidth of an antenna is also used to quantify the range resolution, or the ability discern between two adjacent radar targets [3].

Directivity

Directivity is the ratio of the radiation intensity in a direction to the radiation intensity averaged over all directions. The average radiation intensity is equal to the total power radiated divided by 4π. Directivity (D) in a given direction is found with the following equation:

$$D = \frac{4\pi U}{P_{radiated}} \qquad \text{Eq. 1}$$

where U is the radiation intensity in $\frac{Watts}{solid\ angle}$, $P_{radiated}$ is the total power in $Watts$. Typically, directivity is quoted in the direction of maximum radiation unless otherwise indicated [3].

Gain

Gain and directivity are somewhat related. The difference is gain considers an antenna's directivity in addition to its efficiency. Therefore, gain is the ratio of attained radiation intensity by the antennas in a given direction to the intensity that would be achieved when the power accepted by an antenna is radiated isotropically. For isotropic antennas, the radiation intensity is the power received at the input by the antenna divided by 4π. In equation form, the difference from directivity is using P_{input} instead of $P_{radiated}$ [3].

$$gain = \frac{4\pi U}{P_{input}} \qquad \text{Eq. 2}$$

Bandwidth, and Input Impedance

Antenna bandwidth defines the frequency range over which a chosen antenna characteristic is acceptable, given the desired performance requirement. The most common antenna bandwidth definition is for the input reflection over a given frequency band as characterized by VSWR or S_{11}. Other commonly defined bandwidths are gain pattern, beamwidth, beam direction, sidelobe level, or polarization. For wideband antennas, bandwidth is expressed as the ratio between upper and lower frequencies of the acceptable range. For narrowband antennas, it is quoted as a percentage of the frequency difference (upper minus lower) divided by center frequency of the bandwidth. An acceptable specification for bandwidth cutoff is often decided by convention, depending on the antenna application, more on that below.

VSWR, and S11

The characteristic impedance of (i) the source, (ii) the transmission line connecting the source to the antenna, and (iii) the antenna input port must all be matched to deliver the maximum power to the antenna with low reflection. Input impedance is the ratio of voltage to current at the input terminals of the antenna [1], [3]. An impedance mismatch between the antenna and the characteristic impedance of the feed results in a standing wave along the transmission line (TL) defined by the Standing Wave Ratio (VSWR). Which is the ratio of the partial standing wave's amplitude at a maximum to the amplitude at a minimum along the transmission line, as follows:

$$VSWR = \frac{|\mathrm{V}_{\max}|}{|V_{min}|} = \frac{1 + |\Gamma|}{1 - |\Gamma|} \qquad \text{Eq. 3}$$

where the reflection coefficient (Γ) is the amount of linear mismatch between the antenna impedance (Z_L) and the transmission line impedance (Z_0), as defined by the ratio of the reflected wave to the incident traveling wave:

$$\Gamma = \frac{V_{\text{reflected}}}{V_{\text{incident}}} = \frac{Z_L - Z_0}{Z_L + Z_0} \quad \text{Eq. 4}$$

The reflection coefficient (Γ) is often represented in decibels as S_{11}, for a one-port network such as an antenna both Γ and S_{11} are equivalent, meaning:

$$S_{11} = 20\log|\Gamma| \quad \text{Eq. 5}$$

$$VSWR = \frac{1 + |S_{11}|}{1 - |S_{11}|} \quad \text{Eq. 6}$$

The significance of $VSWR$ and S_{11} as a measure is that the bandwidth of the antenna is defined as the frequency range where S_{11} is less than -10 dB or VSWR is less than 2.

Efficiency

Antenna efficiency (e_0) is a value of losses that an excitation undergoes at the input terminals within the structure of the antenna, as depicted in Figure 2 [3]. Losses that must be accounted for when calculating efficiency are losses from reflections due to input mismatch, dielectric losses (due to the $\tan\delta$ of the dielectric material), and Ohmic losses. The total antenna efficiency (e_0) is calculated by,

$$e_0 = e_r e_{cd} \quad \text{Eq. 7}$$

Where

e_0 = total antenna efficiency

e_{cd} = radiation efficiency

e_r = efficiency due to reflection mismatch $= (1 - |\Gamma|^2)$

Γ = voltage reflection coefficient at the input terminals of the antenna

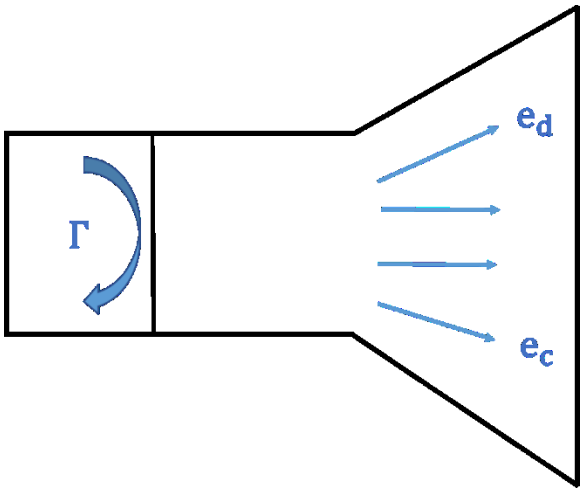

Figure 2. Reflection, dielectric and ohmic losses

Radiation Efficiency

The radiation efficiency (e_{cd}) is formed from the dielectric and ohmic losses together since they are hard to compute and, in most cases, are measured [3]. When using measurements, its complex to separate dielectric from conductive losses, so they are lumped together in e_{cd} [1], which is calculated by

$$e_{cd} = \frac{R_r}{R_{Loss} + R_r} \qquad \text{Eq. 8}$$

where,

e_{cd} = antenna radiation efficiency

R_r= lumped representation of radiation resistance

R_{Loss}= resistance representing dielectric and conductive losses.

Polarization

The polarization of an antenna determines the planar variation of fields of the transmitted signal. Antenna polarization varies with the direction of the antenna. Different lobe points may have different polarizations. In case a direction is not given, the polarization is typically the polarization in the direction of maximum gain [1].

Field Regions

The area around an antenna is subdivided into three regions as a function of distance from the antenna based on the general characteristics of the antenna's radiation in each region: (1) reactive near-field region, (2) radiating near-field region, and (3) far-field region [3]. There are no abrupt transitions in boundaries between the three previously mentioned regions, and some overlap can exist between the three regions. The properties of the three radiation regions are as follows:

1. The reactive near-field region is the "portion of the near-field region immediately surrounding the antenna wherein the reactive field predominates [1]." Generally, the boundary of the reactive near-field is assumed to exist at a distance $R < 0.62\sqrt{D^3/\lambda}$, with λ as the wavelength and D as the antenna's largest dimension [3].

2. The radiating near-field is the region between the reactive near-field region and the proper far-field region, in which radiation fields predominate, and the angular field distribution is dependent on the distance from the antenna [1]. Typically, it starts at $R \geq 0.62\sqrt{D^3/\lambda}$ and ends at $R < 2D^2/\lambda$. This region may or may not exist for some antennas. For example, it may not exist if the antenna's maximum dimension is small compared to the wavelength [3].
3. The far-field is the region where the antenna's field has an angular distribution that is independent of the distance from the antenna, that is the radiation is uniform beyond the far-field's staring boundary [1], [4]. The far-field is defined as $\mathrm{R} = \frac{2\mathrm{D}^2}{\lambda}$, where R must be at a minimum of $\mathrm{R} > 5\mathrm{D}$ and $\mathrm{R} > 1.6\,\lambda$ [4]. The three conditions ensure far-field conditions for many classes of antennas in free space.

Antennas in Short-Pulse Systems

Ultra-wideband (UWB) technologies use short-pulse waveforms in the time-domain that have spectral components occupying a sizeable fractional bandwidth compared to their center frequency. The pulse width of UWB systems can be on the order of hundreds of picoseconds to a few nanoseconds and relative bandwidth exceeding 20% [5]. For this thesis, the two terms UWB and short-pulse, are equivalent.

Many UWB applications use baseband signals, that is, a carrier frequency is not needed, and the signal travels through different mediums depending on its spectral components, where the lower frequency components allow for robust transmission through a variety of mediums [6]. Antenna performance is especially crucial in UWB applications since

such systems operate over a large fractional bandwidth, and antenna performance tends to vary with frequency [5].

UWB systems have found many applications, including high throughput data links, defense applications, impulse radar, precision locating, and medical diagnostics. Some UWB systems can share the spectrum with other UWB, and narrowband users by using low power levels to transmit and receive the information spread over a broad bandwidth [7]. Advantages of UWB Systems include [5], [8], [9]:

- Fine Spatial Resolution – lower λ leads to finer resolution based on the Rayleigh criterion.
- Lower average power – due to the short duty cycle
- Covert operation – robustness to jamming
- High Data Throughput – High data rates in communication applications

Systems are designed to be UWB for a perceived advantage that the short-pulse or the higher bandwidth of the signal provides to the application. In the case of radar, that may be a better range at the same power level or better spatial resolution [8]. One disadvantage is the wide frequency bands of short-pulse excitations can be potentially problematic from a compliance point of view, so careful attention must be given, so the spectrum the signal occupies does not overlap with other broadcasting channels [7]. The Federal Communications Commission (FCC) restricts UWB radio operation to the 3.1–10.6 GHz band, given the signals are at low enough power levels over the allowed band. The large signal bandwidth provides a fine (small step) time and spatial resolution, and the low-frequency

components allow propagation through a range of materials. The challenge is then maximizing the performance given the regulatory constraints and technical tradeoffs of the system design. UWB systems often do not use a standard carrier frequency to establish the RF link or range finding. Instead, they use short-pulse baseband transient pulses [6].

Friis transmission equation

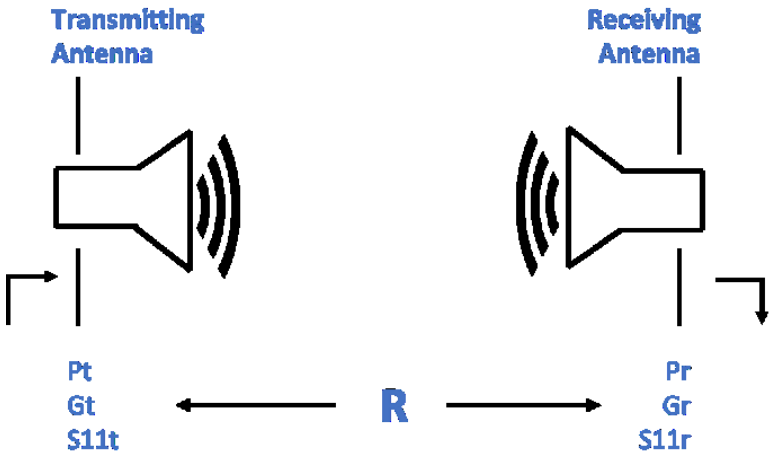

Figure 3. Friis Equation

The Friis transmission equation is a relationship describing the power received by antenna B due to the energy radiated by antenna A, as illustrated in Figure 3. The Friis model is used to represent a simple communication system chain. Where Pt, Gt, and S11t represent transmitted power, gain, and reflected power measured at the transmitting antenna respectively, and Pr, Gr, and S11r for the receiving end.

Eq. 9 is the simplest form of the Friis equation for two antennas in free space where the power at the receiver antenna can be represented as the cascade of the different antenna gains, frequency (wavelength), distance, and the reflection coefficients [3].

$$P_r = G_t G_r \left(\frac{\lambda}{4\pi R}\right)^2 (1 - |\Gamma_t|^2)(1 - |\Gamma_r|^2) P_t \quad \text{Eq. 9}$$

In this thesis, the Friis model will serve as the bases for the abstraction of an antenna as a component of a more extensive electromagnetic system. Chapter 2 will explore that abstraction as described in both the time-domain and the frequency-domain. The respective antenna performance parameters are then discussed.

Survey of Antennas for Short Pulse Applications

While there is a choice of wideband antennas for use in continuous wave (CW), not all antennas are suitable for use with a transient waveform. Transient antennas should be wideband enough to accommodate the spectral components and should not cause disperse the short-pulse excitation, that is, distort its shape and spectral properties. This property is discussed in more detail in Chapter 2. The Log-Periodic (LP) is discussed later as an example of a dispersive antenna with a wide bandwidth that is unsuitable for short-pulse applications where the preservation of the pulse waveform is essential. Other antennas commonly used in short-pulse-UWB applications include the horn antenna, several types of traveling wave antennas, and electrically small antennas.

Helical

The helical antenna is adaptable to many applications, and it has been used in several impulse excited systems [10], [11]. The advantages of the helical antenna include elliptical polarization, wide bandwidth, flexibility of tuning far-field gain, and the possibility of several

modes of radiation. Further, a helical element can radiate RHS or LHS elliptical polarization based on the direction of the helix growth angle.

This thesis is dedicated to optimizing the time-domain performance of a helical antenna such as minimizing pulse spreading in the time-domain while reducing size footprint and maximizing gain. Chapter 4 goes into the helical antenna in more depth, and Chapter 5 systematically studies the different design parameters. The final optimized design is presented in Chapter 6.

Horn

The horn antenna is a versatile radiator made up of a circular or rectangular hollow metallic tube, which is tapered (flared) into a larger opening [3], [12]. The geometry of the tapper defines the performance of the radiator. The popularity of the horn antenna is due to its ease of fabrication, ease of excitation (via waveguide or coaxial), and large gain [3]. Drawbacks of horn antennas in short-pulse applications include that each spectral component is transmitted from a different phase center, which causes high dispersion of the signal, or if coaxial feeding is used, then the balun limits the bandwidth and power levels [13].

There are several types of horn antennas, so the size and performance vary greatly. The pyramidal horn or the horn-ridge antennas are very popular and easy to design but are heavy and large in size. An example of a horn fed antenna that improves performance and size is the Impulse Radiating Antenna (IRA). The IRA archives consistent high gain, large bandwidth, excellent short-pulse performance, and small size [13], [14]. The IRA is a parabolic

reflector fed with a UWB voltage source at the focal point of the reflector, where a TEM horn is formed between the horn feed and the reflector [12].

Valentine Antenna

The Valentine is a traveling wave antenna that combines concepts from the Vivaldi, and balanced TEM Horn. Where the wave travels along the antenna feed with a line impedance of 50Ω slowly reaching the free space impedance of $120\pi\ \Omega$ towards the curved end. The antenna feed is symmetrical strip TL with a dielectric in between. The conductors continue to expand until they meet back at the input port. The dielectric insulation for short-pulse applications is essential; often, oil or other robust dielectrics are used. The Valentine antenna is only capable of linear polarization and has been widely used for sub-nanosecond high power applications [13].

Small EZ Antenna

Electrically small antennas are valuable at lower RF frequencies, where the wavelength is typically large, causing the size and weight of the antennas to be too large for many applications. An antenna is considered electrically small when the values of $ka<0.5$, where $k=2\pi/\lambda$ [15].

The EZ antenna is based on using resonant metamaterials coupled in the far-field to another antenna allowing enhanced antenna behavior at a much smaller size. Their name, according to the inventors, comes from the word easy, for the ease of design and fabricate [16]. Their much smaller size is achieved by filling the space around an antenna with a specially designed metamaterial that is conjugate matched to the inner antenna [15]. The EZ

antenna uses a capacitively-loaded loop placed in the near-field of a classic magnetic dipole. The combined antenna with the surrounding material has been shown to have efficiencies of greater than 90% while maintaining ka<0.5 satisfying the condition for an electrically small antenna [15].

The printed planar compact broadband antenna

The advantage of printed planar compact broadband antennas is that they typically cover a broad range of frequencies and is therefore capable of operating at multiple communication bands, from GPS to WLAN, with a compact antenna size. The standard design consists of an S-strip and a T-strip section printed on the two sides where the side for T-strip is on the front and the S-strip on the backside as a GND plane with a dielectric in between. The top side is terminated at 50 Ω microstrip line, and the bottom side is the ground plane net. The small size of the planar antenna is due to the folding of the S-strip and T-strip meander. Further, the wideband performance is a result of the mutual coupling between the S-strip and the T-strip sections [17].

Summary

In this chapter, we presented the motivation of this work, reviewed basic definitions, and figures of merit for characterizing antenna performance. Prominent figures of merit were gain, directivity, efficiency, and polarization. A brief review of a few UWB antennas was also presented as an introduction for the antenna designs to be considered in this work.

CHAPTER 2

PERFORMANCE ANALYSIS FOR SHORT PULSE APPLICATIONS

In UWB systems with short-pulse excitations, the antenna needs to maintain its properties, within the specified level, over a much broader frequency range than that necessary for narrowband antennas used for typical RF applications. Narrowband antennas can be characterized using the center frequency since many applications are constrained to a small predefined frequency bandwidth around this center frequency. Therefore, performance parameters at the center frequency can be used to estimate the response over the entire frequency band, and time-domain properties are not explicitly considered. In UWB antennas, performance can vary significantly over the bandwidth of the antenna, and since short-pulse signals occupy a large bandwidth, the antenna itself may alter the waveform in several ways.

The short-pulse signal exciting a UWB antenna is subject to differentiation, dispersion (energy storage), radiation, and losses (both dielectric and ohmic). Typically, if the frequency domain response of an antenna is known, its time-domain response can be obtained by inverse Fourier Transform and vice versa. However, specific antenna performance metrics are more conveniently visualized or calculated in one domain over the other. Therefore, both time and frequency domain properties must be considered during the design of a UWB antenna [18].

UWB Signals

Many short-pulses can be used to characterize the time-domain response of UWB antennas.[7] One of the most commonly used baseband signals is the frequency-translated gaussian pulse shown in Eq. 10 [19].

$$v_g(t) = v_{BB}(t)\cos\omega_c\, t \text{ (In terms of cosine)}$$
$$v_g(t) = v_{BB}(t)\sin\omega_c\, t \text{ (In terms of sine)} \qquad \text{Eq. 10}$$

where $\omega_c = 2\pi f_c$ is the frequency of modulation, and $v_{BB}(t)$ is the DC-centered Gaussian pulse. The baseband waveform $v_{BB}(t)$ and its Fourier transform $V_{BB}(\omega)$ are can be described by:

$$v_{BB}(t) = \frac{1}{\sqrt{2\pi}\tau} e^{-t^2/2\tau^2}$$
$$V_{BB}(\omega) = e^{-\tau^2\omega^2/2} \qquad \text{Eq. 11}$$

where τ is the time-domain width of the signal and its spectrum in the frequency domain (FD). So, we can write the frequency domain expressions for $V_g(\omega)$ are given by [19]:

$$V_g(\omega) = \frac{V_{BB}(\omega-\omega_c) + V_{BB}(\omega+\omega_c)}{2} \text{ (In terms of cosine)}$$
$$V_g(\omega) = \frac{V_{BB}(\omega-\omega_c) - V_{BB}(\omega+\omega_c)}{j2} \text{ (In terms of sine)} \qquad \text{Eq. 12}$$

Figure 4 below, shows a sinusoidally modulated Gaussian pulse centered (f_c) around 1 GHz with a bandwidth (BW) of 50% and another sinusoidally modulated Gaussian pulse with f_c at 1 GHz and a BW of 90%.

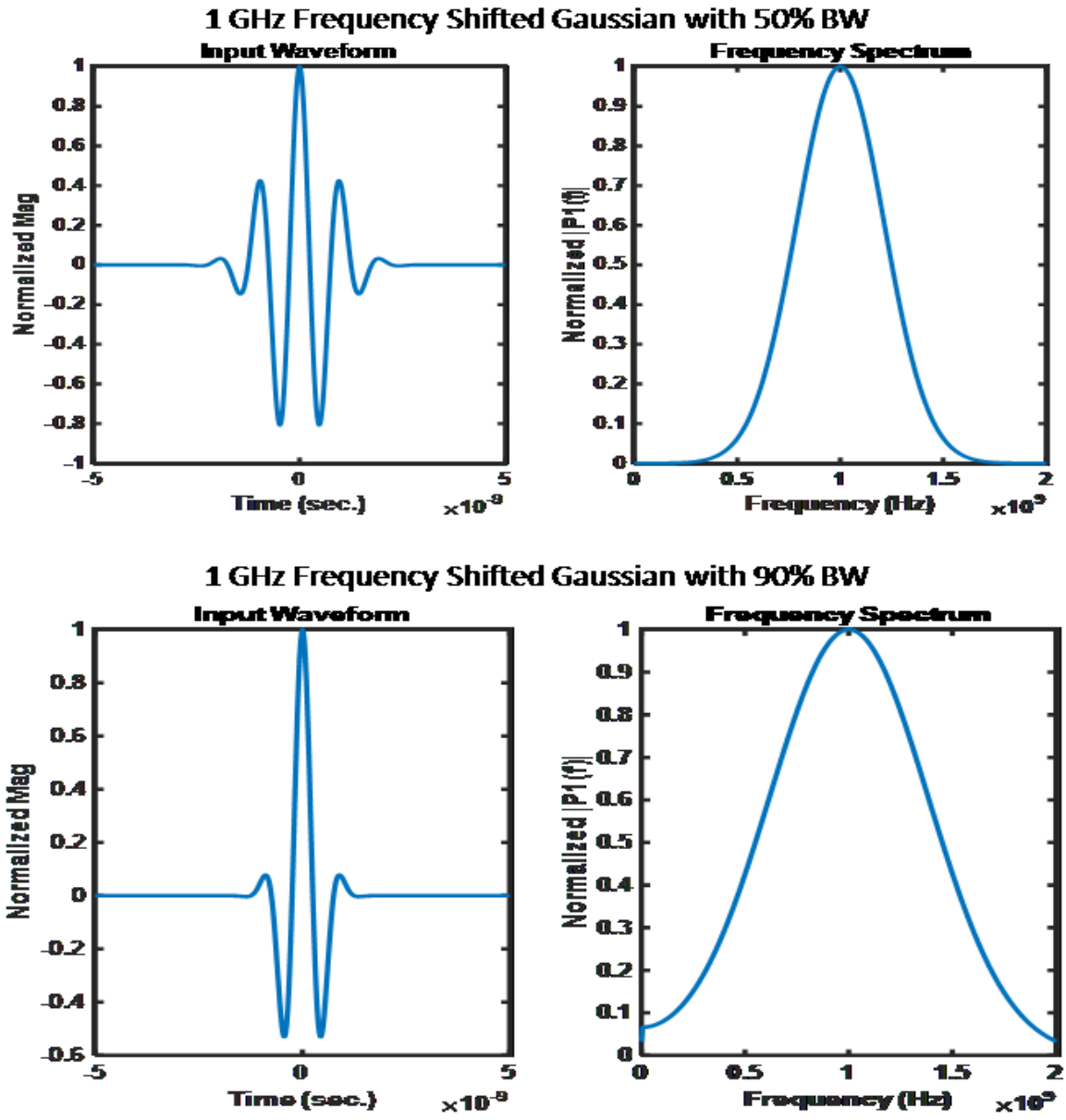

Figure 4. Example of UWB signal in the (a) time-domain (b) and frequency domain

The two signals in Figure 4 will be used in later chapters as the standard time-domain signals to characterize short-pulse antenna performance for the antennas analyzed in this thesis. These signals were chosen because of their well-defined frequency spectrum, their frequent use in UWB systems, their simplicity, and ability to express in closed-form expression both its frequency and time domain profiles [19]. Two different bandwidth

options for the signal are used to test the response of different antennas within and outside their operational bandwidth.

Frequency Domain Performance

Since antennas are passive components, linear time-invariant theory can describe the two-antenna system in Figure 5 [1], with two transfer functions, one for the Tx antenna and another for the Rx antenna similar to the Friis equation discussed in Chapter 1. To comprehensively describe the FD behavior of the antenna, each input and performance parameter must be represented as a multi-dimensional vector to represent the 3-dimensional directionality of an antenna, its frequency, polarization, and range dependence.

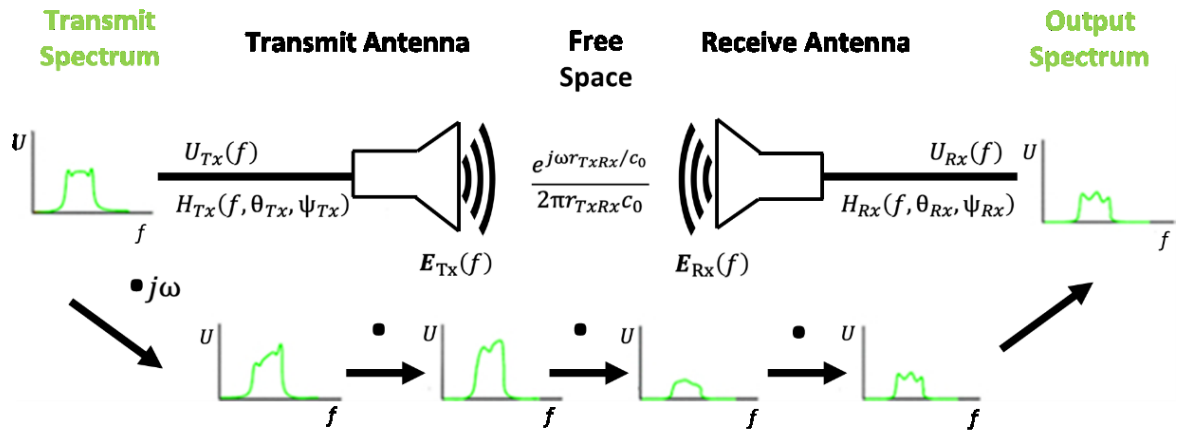

Figure 5. Frequency-domain system link-level characterization [5]

Figure 5 shows the frequency domain representation for a simple two-antenna link where:

- $U_{\mathrm{Tx}}(f)$ and $U_{\mathrm{Rx}}(f)$ are voltage amplitudes at the feed ports for the transmit and receive antennas respectively for a given frequency in volts
- $G(f,\theta,\psi)$ is the gain at a given frequency in the (θ,ψ) direction

- $Z_{\mathrm{C,Tx}}(f)$ and $Z_{\mathrm{C,Rx}}(f)$ are the characteristic impedance at the antenna propagating medium interface
- r_{TxRx} is the distance between the transmitting and receiving antennas
- $E_{\mathrm{Tx}}(f, r, \theta_{\mathrm{Tx}}, \psi_{\mathrm{Tx}})$ is the radiated electric field due to the transmit antenna at location r
- $H_{\mathrm{Tx}}(f, \theta_{\mathrm{Tx}}, \psi_{\mathrm{Tx}})$ and $H_{\mathrm{Rx}}(f, \theta_{\mathrm{Rx}}, \psi_{\mathrm{Rx}})$ are the antenna transfer functions in meters, i.e., frequency-dependent effective length [20]

Figure 5 can be viewed as a cascade of subsystems seen by the signal path from right to left. In the frequency domain, the output field ($E_{\mathrm{Tx}}(f, r)$) at a point $\boldsymbol{r}$ due to the input voltage $U_{Tx}(f)$, can be expressed in the frequency domain by the multiplication of the response of different subsystems as [5]:

$$\frac{E_{\mathrm{Tx}}(f, r)}{\sqrt{Z_0}} = \frac{e^{j\omega r_{TxRx}/c_0}}{2\pi r_{TxRx} c_0} H_{Tx}(f, \theta_{Tx}, \psi_{Tx}) \cdot j\omega \frac{U_{Tx}(f)}{\sqrt{Z_{C,Tx}}} \qquad \text{Eq. 13}$$

To solve for the frequency domain transfer function of the antenna alone. Eq. 13 can be rearranged into the ratio of the field at a distance to the input voltage to the antenna, as shown in Eq. 14, to characterize the first half of the two-antenna link.

$$\boldsymbol{H}_{Tx}(f, \theta_{Tx}, \psi_{Tx}) = \frac{Output}{Input} = \frac{\boldsymbol{E}_{\mathrm{Tx}}(f, \boldsymbol{r}) \cdot 2\pi r_{TxRx} c_0 \cdot \sqrt{Z_{C,Tx}}}{j\omega\, U_{Tx}(f) \cdot e^{j\omega r_{TxRx}/c_0} \cdot \sqrt{Z_0}} \qquad \text{Eq. 14}$$

In the receive mode, Eq. 15 describes the input voltage at the Rx antenna's port due to the field by the Tx antenna, $E_{\mathrm{Tx}}(f, r)$. $\mathbf{H}_{Rx}^{\mathrm{T}}(f, \theta_{Rx}, \psi_{Rx})$ describes the behavior of the receiving antenna, which can be cascaded with Eq. 13 to get the antenna's response due to

the presence of an electrical field. This simple description can be used in the frequency domain to characterize the system and solve for all the relevant parameters fully.

$$\frac{U_{Rx}(f)}{\sqrt{Z_{C,Rx}}} = \mathbf{H}_{Rx}^{\mathrm{T}}(f, \theta_{Rx}, \psi_{Rx}) \cdot \frac{e^{j\omega r_{TxRx}/c_0}}{2\pi r_{TxRx} c_0} \cdot \mathbf{H}_{Tx}(f, \theta_{Tx}, \psi_{Tx}) \cdot j\omega \frac{U_{Tx}(f)}{\sqrt{Z_{C,Tx}}} \quad \text{Eq. 15}$$

Group Delay

A critical frequency domain performance parameter for UWB antennas is the group delay, τ_g which assesses the levelness of the derivative of the phase of the radiated signal as:

$$\tau_{\mathrm{g}}(\omega) = -\frac{d\varphi(\omega)}{d\omega} \quad \text{Eq. 16}$$

Group delay is sometimes expressed as the mean group delay, $\overline{\tau_{\mathrm{g}}}$, over the antenna bandwidth as a single number spec for comparing antennas different antennas:

$$\overline{\tau_{\mathrm{g}}} = \frac{1}{\omega_2 - \omega_1} \int_{\omega_1}^{\omega_2} \tau_{\mathrm{g}}(\omega) d\omega \quad \text{Eq. 17}$$

In any system, different frequency components of a signal are delayed due to the propagation length and type of medium. It is often preferable that the group delay is the same across the bandwidth, that is, the antenna has a linear phase, but in many practical antennas, the delay is different for different spectral components. This variation leads to high distortion in short-pulse signals since their constituent components are not delayed by the same amount of time throughout the antenna structure. This distortion can change the shape of the original waveform, input to the antenna, in addition to the expected dielectric and ohmic losses to the radiated pulse.

The accepted group delay variations depend on the intended application. Some systems implement circuitry or digital signal processing techniques to compensate for pulse shape distortions. For example, UWB radio receivers use impulse correlators to define the similarity between the signal received and a known template signal [19]. In some UWB applications, it is impractical to reconstruct the signal. So, a pulse preserving antenna is of great importance to system performance.

Fidelity Factor

Even though the mean group delay roughly represents the group delay performance of an antenna in a single number, comparing antennas strictly based on an acceptable $\overline{\tau_g}$ value can be misleading. Since $\overline{\tau_g}$ does not provide information on the deterioration of a practical input pulse. The antenna Fidelity Factor ($\boldsymbol{FF}$) measures how close the radiated time-domain field waveform $\boldsymbol{e}_{Tx}(t, \boldsymbol{r})$ of a transmitting antenna resembles the driving time-domain voltage $u_{Tx}(t)$ [6], [19]. By convention, a pulse transmitting antenna is said to have satisfactory pulse preserving properties if the fidelity factor is greater than 0.9 [21], [22]. In the time domain, the FF can be calculated as follows [19]:

$$\boldsymbol{FF} = \max_{t} \frac{\left| \int_{-\infty}^{\infty} \boldsymbol{e}_{Tx}(t' + t, \boldsymbol{r}) u_{Tx}(t') dt' \right|}{\sqrt{\int_{-\infty}^{\infty} |\boldsymbol{e}_{Tx}(t', \boldsymbol{r})|^2 \, dt'} \sqrt{\int_{-\infty}^{\infty} |u_{Tx}(t')|^2 \, dt'}} \qquad \text{Eq. 18}$$

The radiated electric field from the antenna $\boldsymbol{e}_{Tx}(\mathrm{t}, \boldsymbol{r})$, requires a finite delay time to reach the observation point *r*. This delay is difficult to predict beforehand because it depends on the antenna and the distance between the antenna and the observation point. Therefore, the numerator of the equation above performs the cross-correlation between $\boldsymbol{e}_{Tx}(t, \boldsymbol{r})$ and the

input voltage to the antenna, $u_{Tx}(t)$, for different time delays, and the "max" operation is used to select the maximum value of this cross-correlation. This maximum value occurs at the time delay where $\boldsymbol{e}_{Tx}(\mathrm{t},\boldsymbol{r})$ is closest in shape and properties to $u_{Tx}(t)$.

To transform the expression in Eq. 19 from the time-domain to the frequency-domain, the integral in the numerator of Eq. 18 will be denoted by $\mathrm{c}(\mathbf{r},\mathbf{t})$. Then, it can be transformed into the frequency domain by the Fourier transform to get to $C(\boldsymbol{r},f)$ which can be written as [19]:

$$\begin{aligned} C(r,f) &= \int_{-\infty}^{\infty}\int_{-\infty}^{\infty} \boldsymbol{e}_{Tx}(t'+t,\boldsymbol{r})u_{Tx}(t')dt'\, e^{-j2\pi ft}dt \\ &= \int_{-\infty}^{\infty} \boldsymbol{e}_{Tx}(t'',r)e^{-j2\pi ft''}\,dt'' \cdot \int_{-\infty}^{\infty} u_{Tx}(t')e^{j2\pi ft'}\,dt' \\ &= E(r,f)U_{Tx}(-f) \\ &= -\frac{\eta}{8\pi cZ_0}\cdot\frac{e^{-j2\pi fr/c}}{r}\mathbf{H}_{Tx}(f,\theta_{Tx},\psi_{Tx})|U_{Tx}(f)|^2 \end{aligned} \qquad \text{Eq. 19}$$

The property $U_{Tx}(-f) = U_{Tx}^{*}(f)$, can be used when real-valued signals are used. It is evident from Eq. 19, that the fidelity factor is independent of the phase of the input pulse signal. The fidelity factor is a function of the radiation direction, as determined by the transfer function $\mathbf{H}_{Tx}(f,\theta_{Tx},\psi_{Tx})$.

The denominator of the FF equation can represent the total energy in the exciting and radiated signals, $u_{Tx}(t)$ and $\boldsymbol{e}_{Tx}(\mathrm{t},\boldsymbol{r})$, respectively. Using Parseval's theorem, where the sum of the spectral energy of a signal in the frequency domain must be equal to the signal's total energy in the time-domain as:

$$\int_{-\infty}^{\infty} |x(t)|^2\, dt = \int_{-\infty}^{\infty} |\mathrm{X}(2\pi f)|^2\, df \qquad \text{Eq. 20}$$

In Eq. 20 above the signals $x(t)$ and $\mathrm{X}(2\pi f)$ are related by the continuous Fourier transform. Therefore, the denominator of Eq. 18 becomes [19]:

$$\sqrt{\int_{-\infty}^{\infty} |\boldsymbol{e}_{Tx}(t', \boldsymbol{r})|^2\, dt'} \sqrt{\int_{-\infty}^{\infty} |u_{Tx}(t')|^2\, dt'} \qquad \text{Eq. 21}$$

$$= \sqrt{\int_{-\infty}^{\infty} |E(r, f)|^2\, df} \sqrt{\int_{-\infty}^{\infty} |U_{Tx}(f)|^2\, df}$$

Combining Eq. 22 with Eq. 20, allows the calculation of the FF using the frequency domain response of the antenna similar to how Eq. 19 allows the calculation of the FF using the time domain response of an antenna.

Time Domain Performance

In the time-domain, the antenna can be treated as a linear system whose response can be modeled using its impulse response [5]. Figure 6 represents an equivalent antenna link in the time-domain with the typical mathematical operations that a Gaussian pulse undergoes in the simple system shown in the small plots.

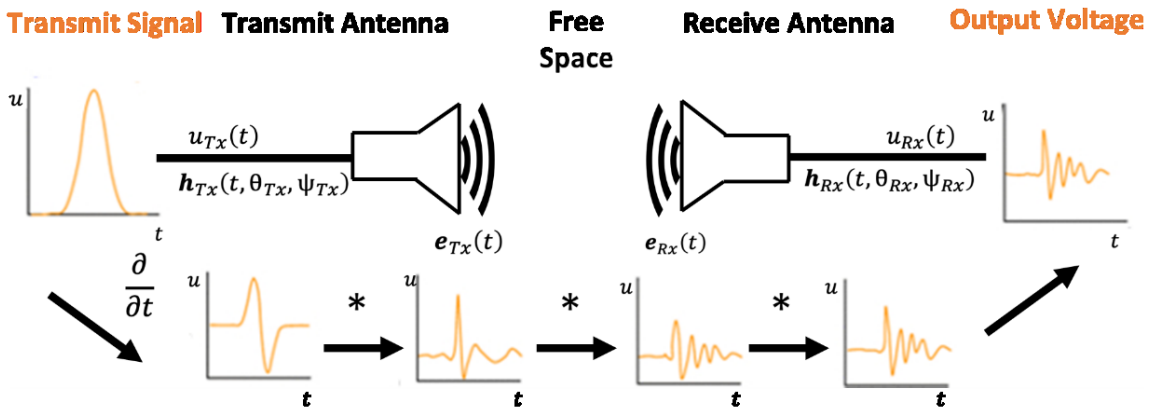

Figure 6. UWB system link-level characterization in the time-domain [5]

In Figure 6,

- r_{TxRx} is the distance between Tx and Rx
- $e_{\mathrm{Tx}}(t, r, \theta_{\mathrm{Tx}}, \psi_{\mathrm{Tx}})$ is the radiated field due to the Tx antenna
- $u_{\mathrm{Tx}}(t)$ and $u_{\mathrm{Rx}}(t)$ are the exciting waveforms for the Tx and Rx antennas respectively
- $\boldsymbol{h}_{\mathrm{T}}(t, \theta_{\mathrm{Tx}}, \psi_{\mathrm{Tx}})$ and $\boldsymbol{h}_{\mathrm{R}}(t, \theta_{\mathrm{Rx}}, \psi_{\mathrm{Rx}})$ are the impulse response in m/ns for the Tx and Rx antennas respectively [20]

The time-domain impulse response for the two antennas can be arrived at by transforming Eq. 13 and Eq. 15 to the time-domain, as shown in Eq. 22 and Eq. 23 below [5]:

$$\frac{\boldsymbol{e}_{Tx}(t, \boldsymbol{r})}{\sqrt{Z_0}} = \frac{1}{2\pi r_{TxRx} c_0} \delta\left(t - \frac{r_{TxRx}}{c_0}\right) * \boldsymbol{h}_{Tx}(t, \theta_{Tx}, \psi_{Tx}) * \frac{\partial}{\partial t} \frac{u_{Tx}(t)}{\sqrt{Z_{C,Tx}}} \quad \text{Eq. 22}$$

$$\frac{u_{Rx}(t)}{\sqrt{Z_{C,Rx}}} = \boldsymbol{h}_{Rx}^{T}(t, \theta_{Rx}, \psi_{Rx}) * \frac{1}{2\pi r_{TxRx} c_0} \delta\left(t - \frac{r_{TxRx}}{c_0}\right) * \boldsymbol{h}_{Tx}(t, \theta_{Tx}, \psi_{Tx}) * \frac{\partial}{\partial t} \frac{u_{Tx}(t)}{\sqrt{Z_{C,Tx}}} \quad \text{Eq. 23}$$

Time-domain parameters of an antenna can be analyzed by looking at the analytic impulse response, which is calculated by the Hilbert transform $\boldsymbol{H}$ such that the analytic impulse is

$$h^{+}(t) = h(t) + jH\{h(t)\} \quad \text{Eq. 24}$$

The envelope of the analytic function, $|h^{+}(t)|$ can also provide a measure of an antenna's dispersion through its peak value and time width at half peak value [5].

Peak Value of the Envelope

The peak value of the envelope of the analytic response is inversely related to the dispersion caused by the antenna because a higher envelope peak value would mean more localization and less spreading of the energy in the time-domain. The peak value of the envelope of the analytic response, $p(\theta, \psi)$, can be expressed as:

$$p(\theta, \psi) = max|h^{+}(t, \theta, \psi)| \quad \text{Eq. 25}$$

The Full Width at Half Maximum Time

The time width of the impulse response at half the peak value can be used to assess the widening of the impulse response due to dispersion in the antenna. Lower FWHM time is typically desired in a UWB antenna, and it can be expressed as [5]:

$$\tau_{\text{FWHM}} = t_{1}|_{|h^{+}(t_1)|=p/2} - t_{2}{}_{t_1<t_2, |h^{+}(t_2)|=p/2} \quad \text{Eq. 26}$$

Ringing

The Ringing time is another parameter that measures oscillations in the radiated pulse beyond the max peak value, which is another critical parameter in the time-domain characterization of UWB antennas [5]. Short ringing time is typically desired. Ringing is defined for a given lower bond ratio, α , with respect to the envelope peak value for a given antenna, such that the lower bound is $\alpha \cdot p(\theta, \psi)$ and ringing time τ_r is [5], [18]:

$$\tau_{r,\alpha} = t_{1}|_{h^{+}(t_1)=\alpha p} - t_{2}|_{t_2<t_1 \wedge h^{+}(t_2)=p} \quad \text{Eq. 27}$$

Summary

UWB systems require robust antenna characterization in both the time and frequency domains, especially when excited using short-pulse (UWB) signals. A discussion on standard UWB signals was presented, followed by relevant UWB frequency and time-domain figures of merit that allow for full characterization of a short-pulse antenna. The figures of merit presented here will be applied in Chapter 5 to the design and analysis of the helical antenna and in Chapter 6 to the optimization of the helical antenna for short-pulse applications.

CHAPTER 3

THE LOG PERIODIC ANTENNA

Frequency Independent antennas

The increase in complexity of radio systems and the continuous demand for a higher transfer data-rates led to an ever-increasing requirement for a wider bandwidth of operation. In many applications such as radar or communications, the use of an antenna that is simple, small, lightweight, and covers the entire frequency band of operation would make both technical and an economic sense. One class of antennas that is typically employed to satisfy all of the previous requirements are frequency-independent antennas (FI), which are used commercially in frequencies that range from 10 MHz to 10 GHz [3].

The motivation behind the use of frequency-independent antennas is to maintain consistent performance along with the band of operation –such as input impedance, max gain, polarization, and radiation patterns. For FI antennas, the antenna performance is invariant if the physical size of the antenna is scaled as the ratio of the operating frequency or wavelength. That is, the electrical size of the radiating feature is kept constant with respect to frequency or wavelength [3], [23]. For example, if all the physical dimensions are doubled, antenna performance will be unchanged if the operating frequency is halved. Using the FI design principles, it is possible to have antennas with up to 40:1 bandwidth ratio or even bandwidth ratios of 1000:1 are achievable [3]. Common FI structures are the spiral antenna and log-periodic antennas [3].

The Planar Log-Periodic Antenna

Log-periodic (LP) antennas consist of several radiating elements scaled by a frequency-independent logarithmic ratio. A classical log-periodic antenna can be fabricated from multiple radiating wires (dipole elements) scaled by a logarithmic ratio [3], [24]. Each radiating item has a narrow bandwidth as defined by the narrow frequency bandwidth, where its input impedance meets the design characteristics. By arranging several logarithmically scaled elements, the log-periodic antenna provides a nearly constant input impedance over the desired bandwidth. Log periodic antennas have been extensively used since the 1960s finding many applications where wide bandwidth, moderate gain (6-12 dBi), and consistent radiation pattern are desired [25].

The LP antenna is commonly used at lower frequency applications, including HF/VHF/UHF bands, for applications such as long-distance broadcasting of radio and television (short waves), home TV reception, wireless communication (base station and relays), and electromagnetic compatibility (EMC) in anechoic chambers. Off the shelf, LP antennas are typically fed with a balun and can sustain continuous power levels in excess of 1 kW. Significant drawbacks to the LP structure are its large size and susceptibility to dispersion [3], [24], [25].

Low-profile LP antennas are typically termed as planar LP antennas, and they are typically etched or printed on a substrate. This results in a much more favorable size that can be used in flush-mounted configuration to a surface. The planar LP has found many applications where a large bandwidth, consistent performance, and proper power handling are essential. An LP slot antenna has demonstrated a sustained continuous power level of

500 W over a prolonged period [26]. The planar LP is typically used at higher frequencies than the classic LP [3]. Figure 7 shows an illustration of a typical planar LP design. The principle of operation log-periodic antenna as a quasi FI antenna is summarized as a structure whose electrical length changes periodically with the logarithm of frequency, such that the impedance and radiation pattern is repeated regularly along the entire bandwidth.

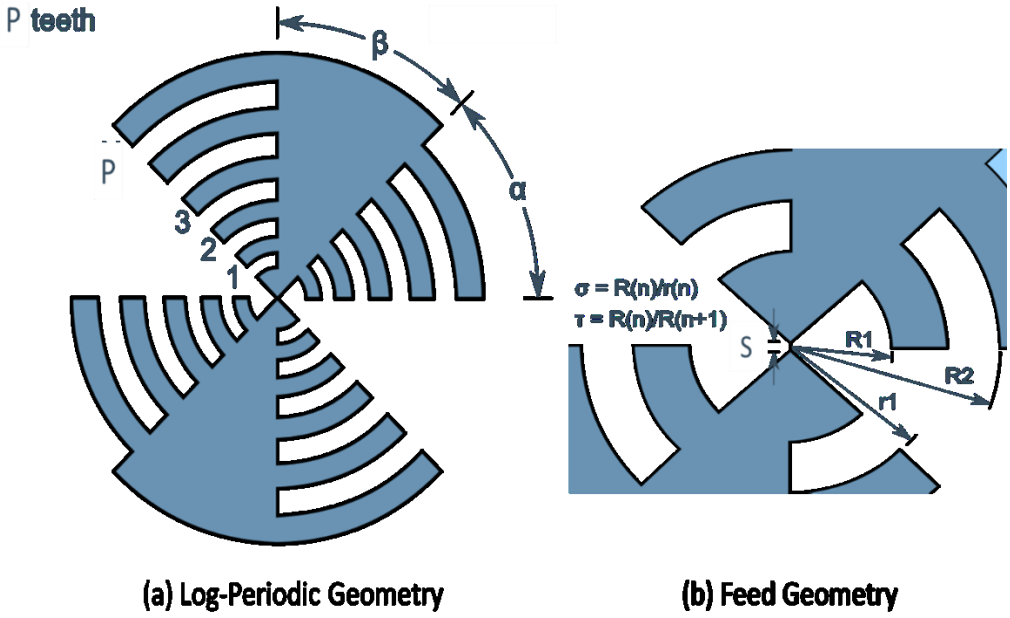

Figure 7. Planar Log-periodic

For the design and analysis of LP antenna, the number of teeth (radiating elements) is termed P, each with a given outer (R_p) and inner (r_p) radius from the origin along a feeding arm. The teeth on these arms radiate best when they are λ/4 long [3]. Therefore, the outermost tooth controls the low-frequency cutoff of the antenna, whereas the innermost tooth governs the highest frequency of operation, consistent with the classical LP [25]. The teeth are numbered from the outermost 1 to the innermost. The radii of the teeth are related

to each other by the growth factor τ, which can be constant or varied across the radiating elements such that [27]:

$$\frac{R_{p+1}}{R_p} = \tau \qquad \text{Eq. 28}$$

The width of each radiating element is determined by σ, such that

$$\frac{r_p}{R_p} = \sigma \qquad \text{Eq. 29}$$

The parameter β is used to describe the arm feed angle, and α is the tooth angle. For a self-complementary structure, the following relationships must hold [27]:

$$\sigma = \tau, \text{ therefore } r_p = R_{p+1}$$

$$a + \beta = \frac{\pi}{N} \qquad \text{Eq. 30}$$

Other important parameters to control are those related to the impedance and bandwidth. The impedance of each arm in a self-complementary antenna is given by

$$Z = \frac{\frac{\eta}{4}}{\sin\left(\frac{m\pi}{N}\right)} \qquad \text{Eq. 31}$$

Such that η is the free space impedance, N is the arms, and m is the mode of operation. The bandwidth of the LP antenna is determined by the tooth angle α , the inner and outermost radii, such that

$$R_1 = \frac{\lambda_{low\ frequency\ cutoff}}{4\ a} \ \ and\ R_p = \frac{\lambda_{highest\ frequency\ cutoff}}{4a} \qquad \text{Eq. 32}$$

Points of interest and a summary of planar LP design parameters are presented in the bullet points below which can be used to tune the antenna response, [3], [24], [25], [27]:

- Planar PL antennas can be built in 2 or 4 arm configurations. The two-arm shape is linearly polarized, as shown in Figure 7, and will be designed in the next section. The four-arm configuration will be discussed later in the chapter; it can be circularly polarized by utilizing a 90-degree phase shift between the feed of the perpendicular arms.
- The minimum frequency can be reduced by increasing the length of the longest radiating element, while the maximum frequency can be increased by shortening the smallest tooth.
- A smaller antenna footprint, i.e., a more compact design, can be achieved by varying the scale factor and tooth to slot ratio for different teeth at the expense of self-complementary and impedance consistency.
- The impedance to the ground of each arm can be increased or decreased by varying the metal to slot ratio. Changing the metal to slot ratio to a value other than one makes the aperture none self-complementary. This may produce the desired average impedance but may introduce higher oscillations in the impedance over a given frequency band. Both designs will be explored in this chapter.
- The tooth angle α can be increased to lower the cutoff frequency of the aperture. If 'α' is enhanced with 'β' unchanged, the metal to slot ratio of the new hole will change, having the effects on impedance and canceling the self-complementary property.

- The growth rate 'τ' can be used to improve the antenna beamwidth; increasing 'τ' increases the beamwidth. A simple explanation of this phenomenon is that higher growth rates lead to narrower active teeth, which leads to lower directivity due to area smaller area from which currents radiate.
- The self-complementary structure allows for a complement of the design to also radiate and operate as an antenna. This provides additional fabrication flexibility when etching the structure onto a copper substrate.
- The simple feeding structure of the antenna positions it well to be used as a part of an antenna array.

Design of a Planar Log-Periodic for Short pulse-UWB Applications

To illustrate the operating principles of the planar log-periodic antenna and explore their suitability for short-pulse-UWB applications, a two-arm helical antenna is designed in FEKO [28]. The design goal is to have an operational bandwidth between at least 700 MHz and 2 GHz, ensuring the input impedance is near $160\ \Omega$ and using a commonly available substrate material. The antenna geometrical properties are summarized in Table 1 below:

Design	*Value*
Scale factor (τ)	.81
Tooth to slot	.90
Feed spacing	1.5 mm
Tooth angle (α)	45 °
Solid angle (β)	45 °
Number of	7
Inner radius	37.5 mm
Substrate	3 mm
Substrate ε_r	2.2

Substrate Diameter	36.2 cm

Table 1. 2-Arm Log-Periodic Design Parameters

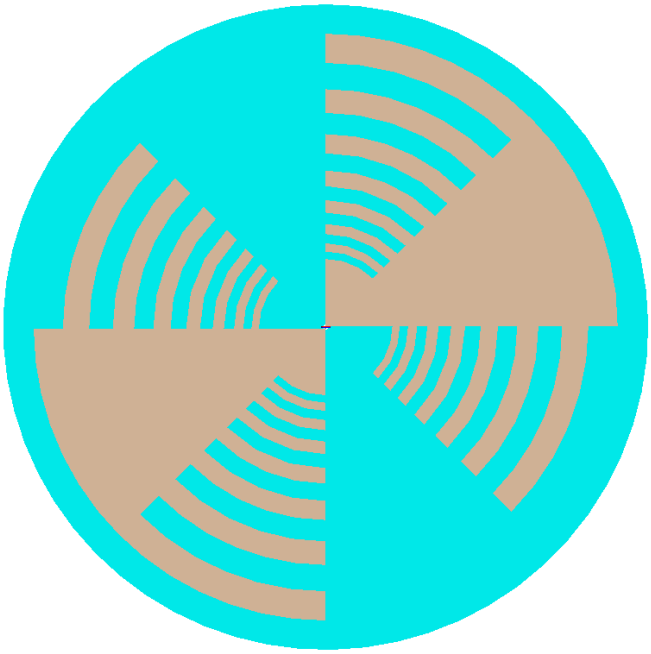

Figure 8. 2-Arm Log-Periodic Antenna

The substrate we opted to use for this design is a Duroid 5880 substrate with $\varepsilon_r = 2.2$. After a couple of design iterations, the design parameters displayed in Table 1 provide an acceptable tradeoff between bandwidth, performance, and size. As shown in Figure 8, and simulated using the FEKO method of moments solver. The 160 to 50 ohms impedance matching section will be discussed in a later chapter; since both the helical and Log-periodic were designed to have a 160-ohm input impedance.

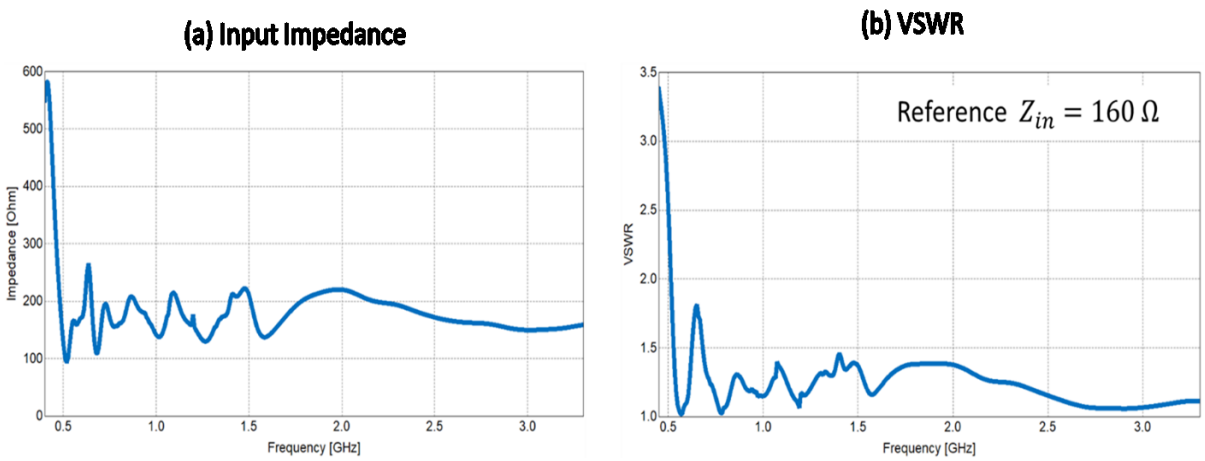

Figure 9. Input Impedance and VSWR for the 2-Arm LP

Figure 9 (a) shows that the designed antenna's input impedance is relatively flat over the desired bandwidth that ranges from 700 MHz and 2 GHz. When using an input impedance of 160 ohms, the antenna is operational over a much wider scale. Figure 9 (b) indicates that the turn-on frequency of the designed antenna is around 500 MHz, and the antenna is operational beyond 3 GHz.

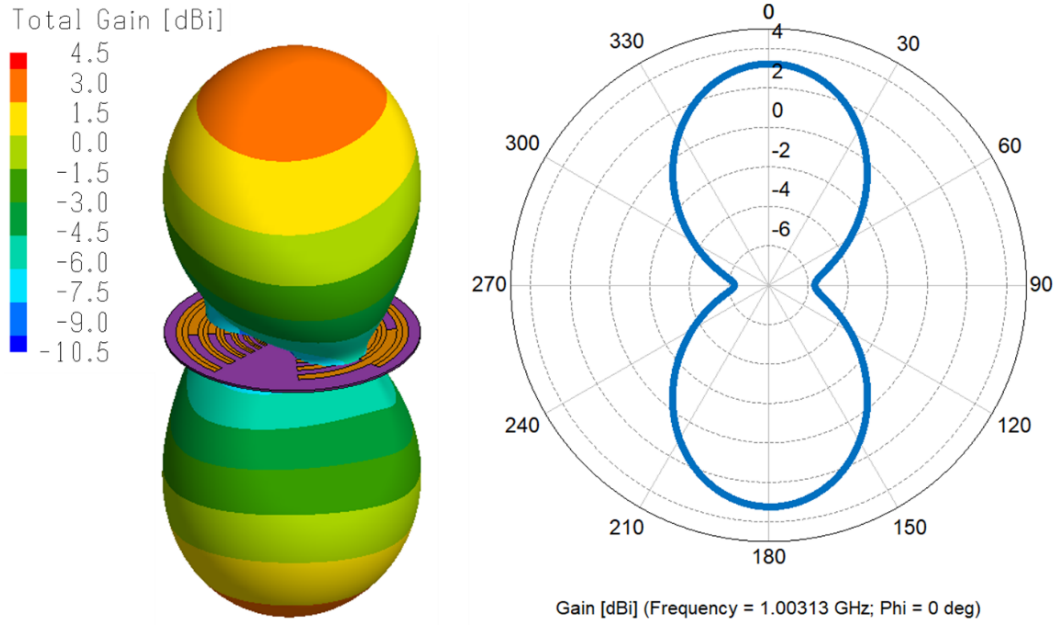

Figure 10. 2-Arm LP Gain Pattern

The gain pattern of the simulated antenna at 1 GHz is shown in Figure 10. The maximum gain value is 3.2 dBi in the boresight direction. The antenna is bi-directional; that is, it radiates in both the backfire and boresight direction. The back lobe is affected by the presence of the RT Duroid dielectric substrate.

Log-Periodic Time-Domain Performance

Even though this antenna provides excellent bandwidth characteristics, this is not sufficient to guarantee that the antenna will be suitable for UWB short-pulse applications. The time-domain performance of the antenna must also be quantified. To that end, the antenna's FEKO transfer function was extracted from the full-wave simulation to MATLAB, then the Fidelity Factor (FF) was characterized in MATLAB, as discussed in Chapter 2.

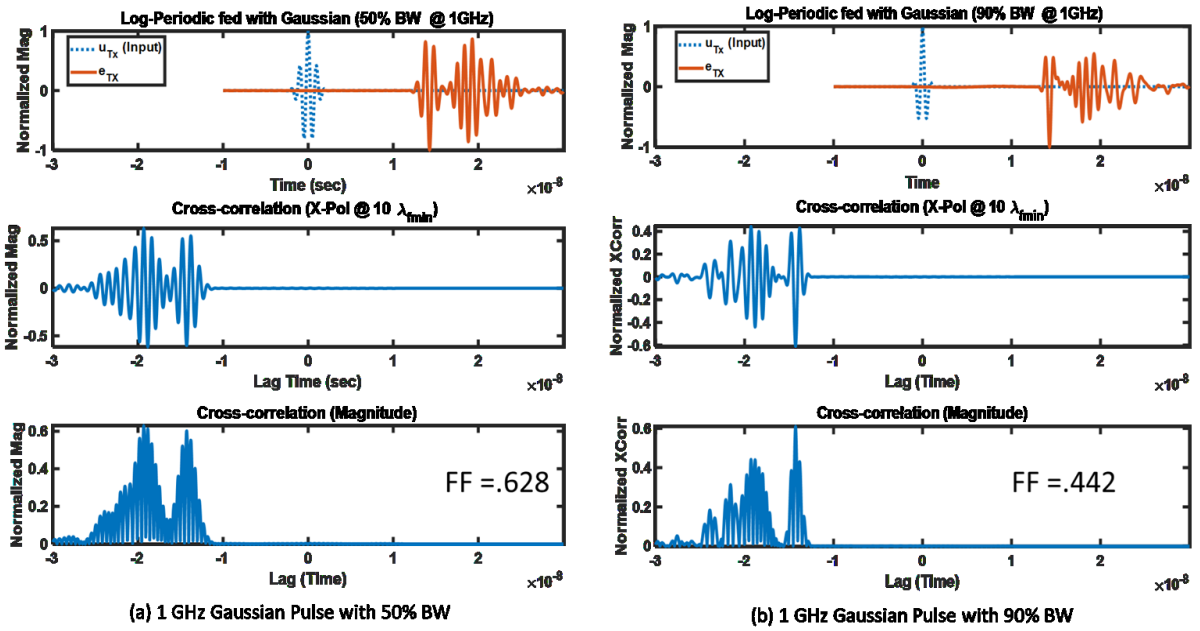

Figure 11. 2-Arm LP Time-Domain Response

The Fidelity Factor is the measure of waveform preservation through the antenna. Figure 11 (top plot) shows the shape of the exciting wave in blue and in orange, the X

polarization of the electric field as measured at a distance of $10\,\lambda$ away from the antenna. Clearly, the radiated pulse differs significantly in shape and duration from the input pulse to the LP antenna. The reason for this pulse distortion is that different parts of the antenna radiate different frequency components of the input pulse. That is, if a pulse with multiple frequency components arrives at the feed of an LP antenna, it will travel through the feed line of the LP to the smallest tooth where the high-frequency components will radiate. At this time instant, the low-frequency components will still be confined within the antenna. These low-frequency components will travel an extra distance that will incur a time delay before they reach the largest tooth. After the signal reaches the largest tooth, it will radiate. Therefore, there will be an added delay between the high and low-frequency components of the pulse, which was not present in the input pulse to the LP antenna. As illustrated in Figure 12, the added delay is what distorts the shape of the pulse [29], [30].

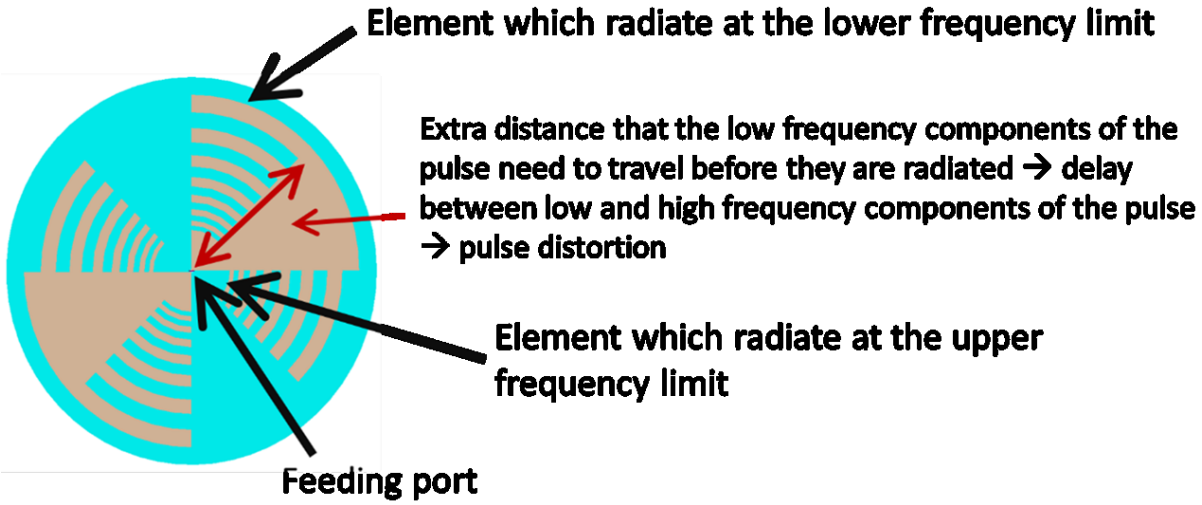

Figure 12. Dispersion in LP Antenna

The middle plot of Figure 11 shows the cross-correlation between the input signal (input waveform) and the output signal (E field at $10\,\lambda$). The magnitude of the cross-

correlation is shown in the bottom plot; the maximum values of the magnitude is the fidelity factor since that value represents the time lag where both signals are at the correct phase (time lag) value to be correlated. An antenna must at least have an FF value of 0.9 to be considered operational in a UWB system for a particular short-pulse excitation. It can be inferred that the Log-periodic antennas shown above are not suitable for short-pulse applications since they distort and disperse the input short-pulse.

Size and Polarization improvement of a Planar Log-Periodic

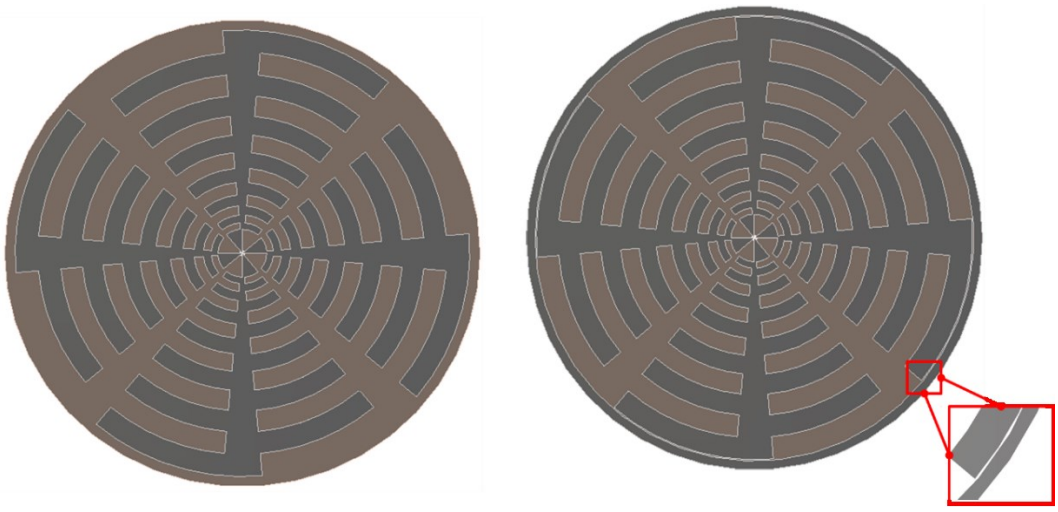

(a) 4-Arm LP antenna **(b) Ring Coupled 4-Arm LP antenna**

Figure 13. 4-Arm LP antenna (b) with and (a) without a coupled ring

As discussed earlier, the active region of a log-periodic antenna is when the contour length of the tooth is approximately λ/4, and the outermost tooth typically corresponds to the lowest frequency. Therefore, typical log-periodic antennas have an outer diameter of approximately $\frac{2\,\lambda_{min}}{3}$ at the lowest operational frequency. Recently, an advance in extending the lower frequency cutoff of a dual-polarized four-arm planar log-periodic was presented by

a UC-Boulder team [23]. They were able to miniaturize the LP antenna by a factor of two by the addition of a coupled ring to the outside of the antenna leading to a total antenna diameter of $\frac{\lambda_{min}}{3}$ [23]. In addition to the size reduction, the presented antenna maintained most of the desirable properties of the 2-arm LP antenna such as the quasi FI behavior, and relatively high power handling capability [23]. However, the 4-arm LP antenna also provides circular polarization in comparison to the linear polarization of the 2-arm.

The beauty of FI antennas is the simplicity of scaling their design to extend the bandwidth. Here we design a size reduced Log-Periodic with a target bandwidth between 500 MHz and 6 GHz, as shown in Figure 13, which shows 4-arm LP with and without the coupled ring. To demonstrate the size reduction of the 4-arm LP, two different antennas were simulated with the design parameters listed in Table 2.

Design Parameter	*Value*
Scale factor (τ)	0.9
Tooth to slot ratio (σ)	0.9
Feed spacing (S)	1 mm
Tooth angle (α)	35 °
Solid angle (β)	10 °
Number of teeth (N)	13
Outer radius (R_{13})	80 mm
Inner radius (R_1)	10.9 mm
Substrate Thickness	3 mm
Substrate ε_r	1.5 mm
Substrate Diameter	167.4 cm
Ring Width	2 mm
Ring Spacing	1.7 mm

Table 2. 4-Arm Log-Periodic Design Parameters

The CST simulation results from the ring coupled four-arm planar log-periodic is displayed in Figure 14. The cut on lower frequency limit of the antenna was reduced from

1260 to 670 MHz. That is a 47% reduction in the cut on frequency, which is equivalent to about the same in terms of antenna size reduction. For the same frequency band, the diameter of two-arm LP without the coupled ring is around $\sim \frac{2\lambda_{min}}{3}$. While for the four-arm LP with the coupled ring the diameter is $\sim \frac{\lambda_{min}}{3}$.

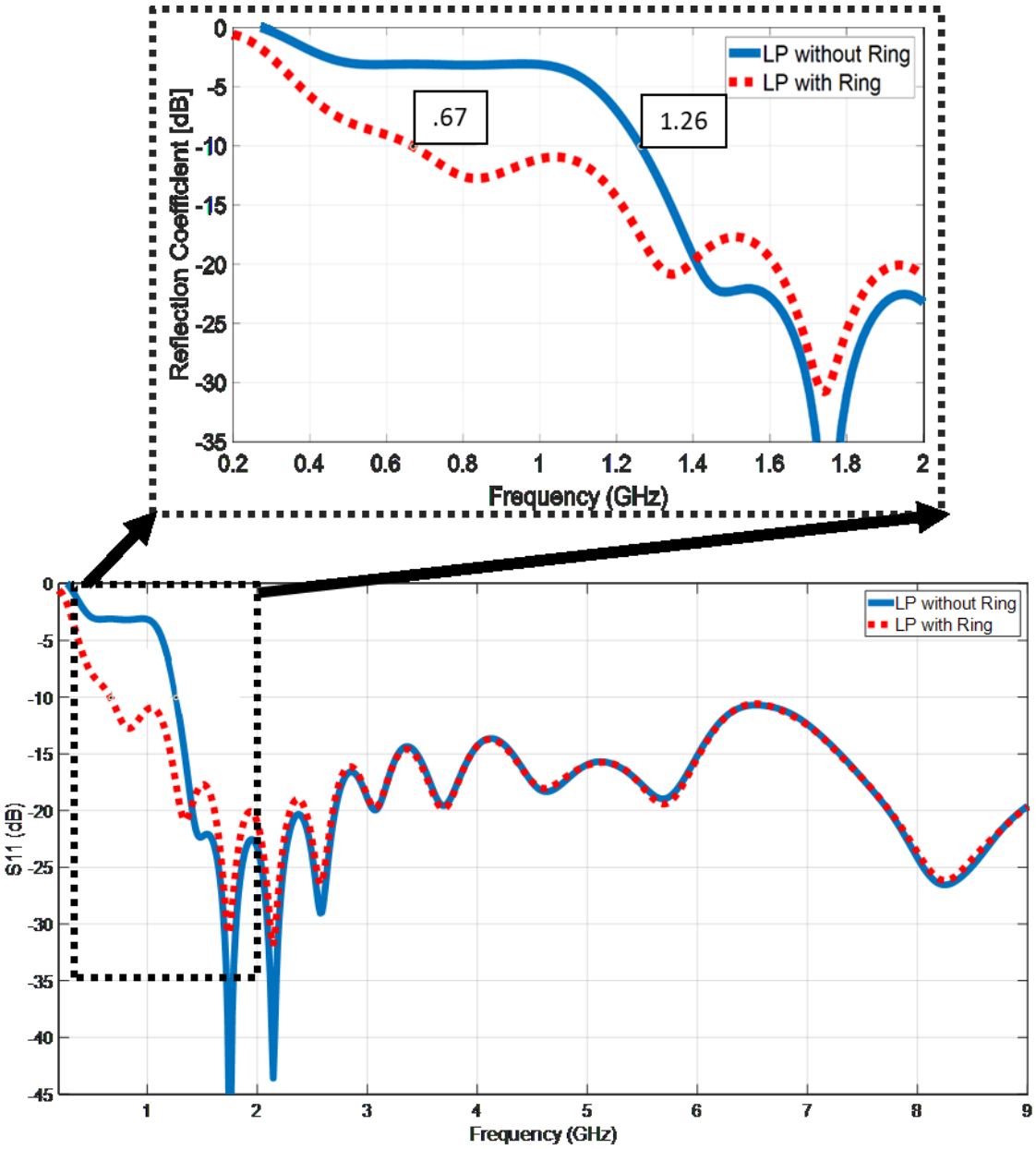

Figure 14. CST Results for the 4-Arm LP with Size Reduction

Summary

This chapter discussed the design of two and four arm planar log-periodic antennas, their suitability for short-pulse applications, as well as a method to reduce the size of a UHF log-periodic antenna. Planar log-periodic antennas have many favorable performance characteristics such as substantial operating bandwidth, flat profile, and flexibility in tuning performance. The time-domain characteristics of planar log-periodic antennas for short-pulse applications remains a significant drawback to their use in pulse preserving UWB systems.

CHAPTER 4
THE HELICAL ANTENNA

Helical antennas seem to perform better in pulse preserving UWB applications than frequency-independent log-periodic antennas. A drawback of the helical antenna is the smaller bandwidth and larger size, but advantages are controllable gain, design flexibility, and high-power capabilities. Helical antenna radiation characteristics can be tuned by controlling its electrical geometry with respect to the wavelength. For example, the gain of the antenna can be increased by increasing the number of turns. Further, the helical antenna is most of the time elliptically polarized, but linear and circular polarization can be achieved at given electrical geometries or frequency bands [3].

In this chapter, we present the geometry of the helical antenna, two validation cases, and discuss applications. In the next two chapters, we further explore the design parameter trade-space and design several antennas suitable for different short-pulse systems.

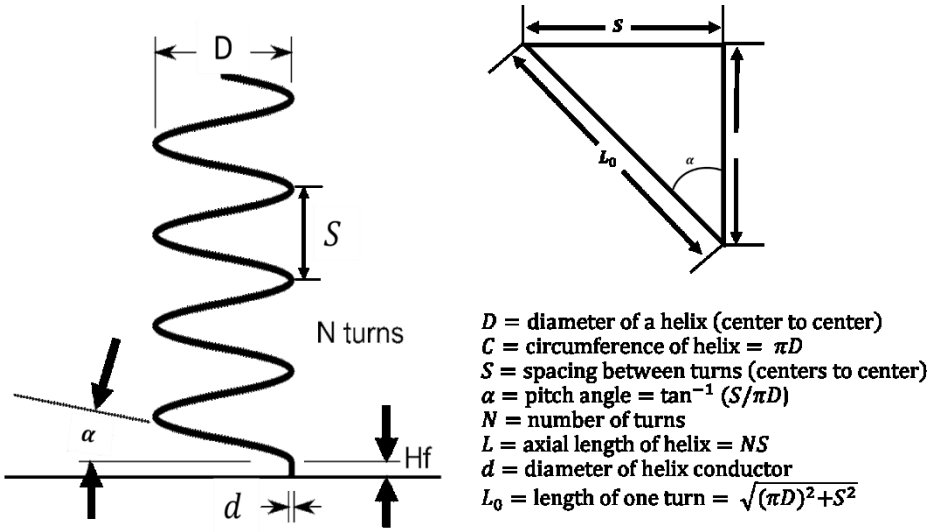

Figure 15. Description of the helical antenna [3]

The geometrical properties of a helical antenna are highlighted in Figure 14. A helical antenna is formed by winding wire with thickness d into a diameter D with a pitch angle α. The pitch angle (α) controls the growth of the wire winding forming a right triangle between the turns (S), helix circumference (C), and the length of one turn (L_o), as shown in Figure 15. The height of the antenna is $L = NS$, while the length of wire required is $L_n = NL_0 = N\sqrt{S^2 + C^2}$ where L_0 is the length of one turn. The angel between turns is

$$\alpha = \tan^{-1}\left(\frac{S}{\pi D}\right) \qquad \text{Eq. 33}$$

Note that when $\alpha = 0°$, the helical is flat reducing it into a loop antenna, and when $\alpha = 90°$ the helical is extended into a wire radiator. Therefore, a helical antenna exists when $0° < \alpha < 90°$.

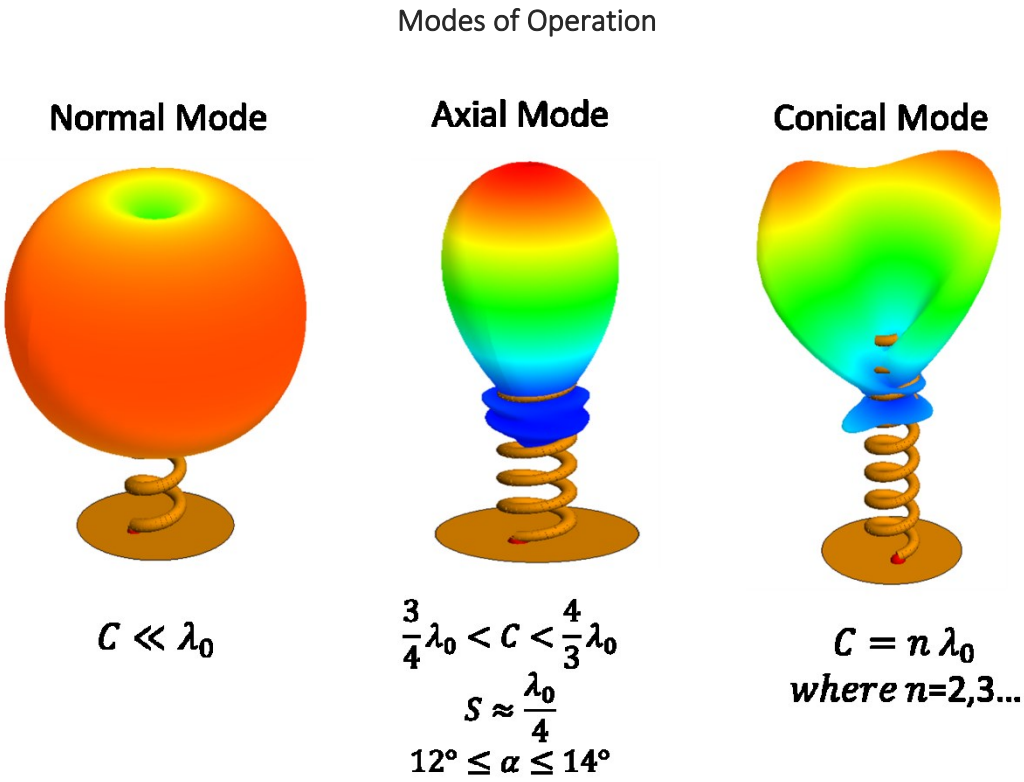

Figure 16. Helical Antenna Modes of operation normal, axial, and conical [2]

Depending on its dimensions relative to its frequency of operation, a helical antenna can to operate in one of the multiple modes with different far-field radiation patterns. Three modes are displayed in Figure 16, the "Normal Mode" where the antenna's circumference is much smaller than the wavelength of interest and the antenna behaves similar to a monopole antenna [3], [31]. The "Axial Mode" of operation is where the major radiation lobe is in the axial direction (also called the boresight mode), and the "Conical mode" which can be viewed as a combination of the two operating modes with multilobe radiation skewed towards the forward direction.

Helical Antenna Applications

One of the most common applications of the normal mode helical antenna is in the "rubber ducky antenna" found in many consumer electronics since the early walkie-talkies to current state of the art public safety communication equipment and Wi-Fi routers [3], [32]. Before the helical antenna was used in the rubber ducky configuration, portable radios used quarter-wave dipole antennas. Early radios operated in the VHF band, causing the whip antenna on portable radios to be as long as 1 m! The rubber ducky is a normal mode helical antenna. The antenna is made of a narrow helix typically with a circumference much less than the wavelength of operation λ_0. The helix is mechanically flexible due to its springy geometry, which is an added advantage making it less prone to damage or breakage than a stiff dipole antenna. The entire helix is typically encased in a plastic case to protect it and a dielectric that can reduce the helix size. The typical rubber ducky antenna is as much as 60% shorter than an equivalent dipole at the same wavelength . $4\lambda < L_n < .15\lambda$ [32].

In a different sphere of applications, the axial (boresight) helical antennas have found many uses in space-based applications both in ground stations and in space payloads in part due to their high gain and polarization. A helical antenna with elliptical polarization can be represented as the superposition of two orthogonal field components in time-phased quadrature. Meaning it can always receive the signals transmitted from a rotating linearly polarized antenna. The polarization advantage, coupled with excellent gain, and tunability led to the widespread adoption of helical antennas in for ground station applications. Helical antennas are often used as a ground transmitter or receiver for signals that must undergo Faraday rotation as they travel through the ionosphere. Such applications included space telemetry, satellites, and space probes [3], [11], [33]–[38].

Antenna Validation

In order to trust our computational simulations, we performed two separate helical antenna design validation cases. In the first validation case, the results from a standard published helical antenna were reconstructed with excellent agreement with the published results. The Second validation case was performed by simulating an identical helical antenna using two separate simulation packages to ensure the robustness of the design and validity of using the modeling tools.

In the first validation case, a helical antenna reported by Topa *et al.* was simulated in FEKO using a coarse mesh with 551 points. The plot shown in Figure 17 shows our reconstructed results, which exhibit excellent agreement with those independently published in [39]. The two plots look very similar; the small variation is believed to be

attributed to the definition of feeding port used and the mesh difference. The paper does not report a port type, but we used a wire port in our simulations. Given the close result attained, we feel comfortable with the results of the validation for this specific design [39].

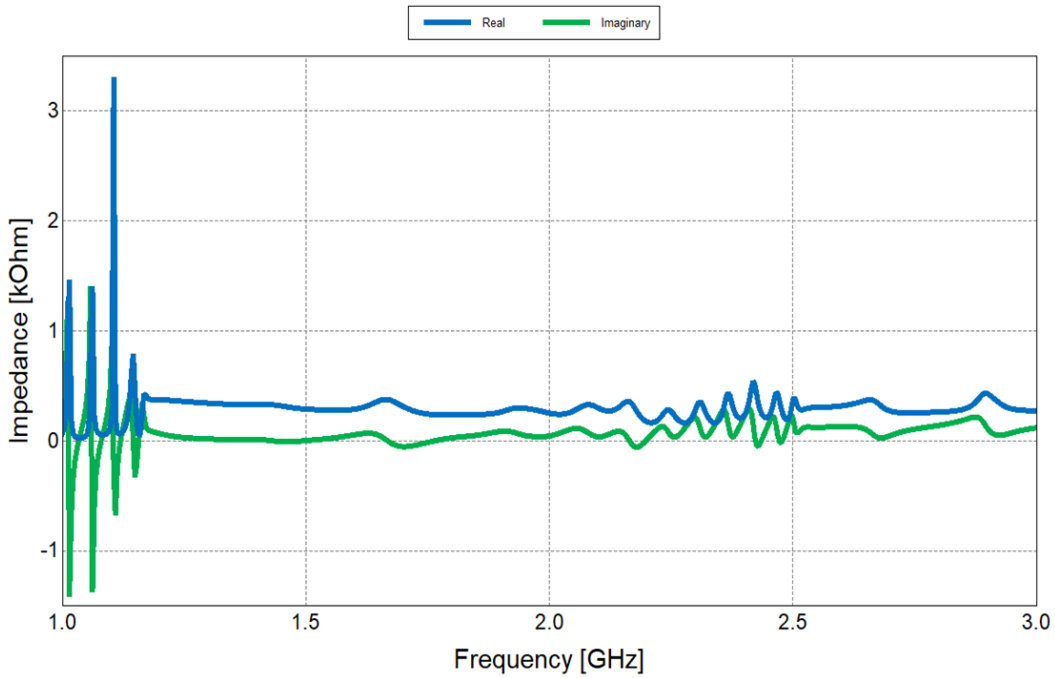

Figure 17. Antenna Validation(FEKO Simulation) [39]

PARAMETER	VALUE
Number of Turns (N)	6
Wire Diameter (D)	3 mm
Ground Plane Diameter (Dg)	749.5 mm
Helix Diameter (D)	238.5 mm
Feed Height (Hf)	30 mm
Pitch Angle (α)	$13°$
Sense	Right-Handed

Table 3. 400 MHz Helical Validation Case

For the second validation case, an axial mode helical antenna was designed to operate at 400 MHz, using the values listed in Table 3. The antenna is simulated in FEKO and the integral equation solver in CST Microwave Studio (MWS) [40], and the reflection at the input

port of the helical antenna is plotted in Figure 18. Both solvers quantitatively agree on the shape and the approximate magnitude of the response. While even more agreement may have been possible with some tweaking; however, the results are satisfactory to validate the design principle and ensure the correct use of the tools.

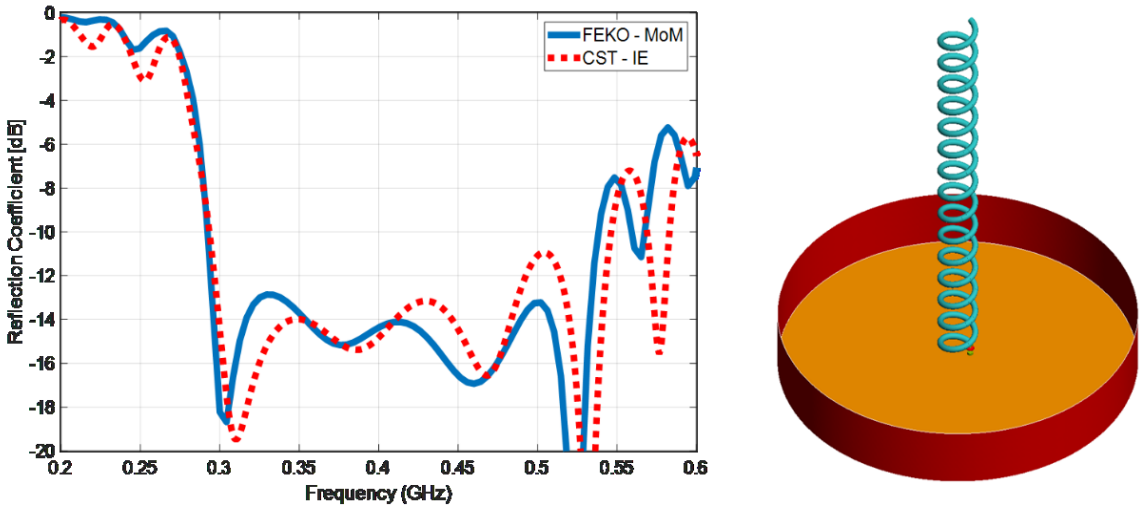

Figure 18. Helical Antenna Validation via CST and FEKO simulations

Helical Antenna Literature Review

A literature review was carried out on axial mode helical antennas via classic helical antenna references and recently reported antenna improvements [10], [11], [41]–[50], [31], [51], [52], [33]–[39]. Here we summarize the many reported results into typical (min through max) performance figures. Reported ranges for helical antenna figures of merit include:

- Elliptical polarization, in both Right and Left Hand sense
- Wide bandwidth (45-60%)
- Useful in UWB short-pulse applications
- Controllable beamwidth (20-60°) and Gain (9-19dBi)
- High power handling ability

- Low complexity, and tolerance to manufacturing variations

Reported disadvantages of the helical antenna include:

- Electrically large (>$\lambda/2$)
- Input impedance between 100-200 Ω

Summary

The helical antenna is a flexible antenna useful for many applications. A helical antenna can be designed to be either omnidirectional or highly directive, depending on the mode of radiation. We performed two independent validation cases. The first case compared a published design to a FEKO simulation, and the second compared the design of the same antenna in CST and again in FEKO.

CHAPTER 5

DESIGN AND PARAMETRIC ANALYSIS OF A HELICAL ANTENNA

This chapter starts from three initial antenna designs based on a previously published study [10], [11], then explores each of the helical antenna designs using full-wave simulations. The contribution of each of the helical antenna's geometrical variables to the antenna performance is discussed and parametrically varied over a reasonably defined domain. The single parameter simulations are run on FEKO using an infinite PEC ground plane to reduce the simulation run time. The second section in this Chapter discusses varying the size of a finite ground plane for the helical antenna to test the effect of the infinite ground plane assumption on the accuracy of the simulation. The results from the parametric study in this chapter will be used to design a suitable antenna for short-pulse applications in Chapter 6.

Antenna Design

Published designs by the Applied Physical Electronics group [10], [11] are used as a starting point for the parametric study and further optimization performed herein. The three initial antenna designs have their center operating frequencies around 400 MHz, 750 MHz, and 1000 MHz, respectively. The helical antennas previously reported employed a conical ground plane [10], [11]. Instead of the conical ground plane reported in [10], [11], we use a flat ground plane to better represent the behavior of the helical antenna without the effect of the cone reflector, which serves to improve gain. The cone reflector can be easily added at a later design stage if necessary.

The reported helical antennas showed a power handling capability of 106 MW from a Marx pulse generator in their outdoor testing [10], [11]. The three antennas are a good starting point for further improvements given that the antennas use a short-pulse excitation and provide high gain.

PARAMETER	400	750	1000
Number of Turns (N)	6	8	8
Wire Diameter (d)	3 mm	3 mm	3 mm
Ground Plane (Dg)	749.5 mm	400 mm	300 mm
Helix Diameter (D)	238.5 mm	127.2 mm	95.43 mm
Feed Height (Hf)	30 mm	16 mm	12 mm
Pitch Angle (α)	$13°$	$13°$	$13°$
Sense	RH	RH	RH

Table 4. Dimensions of initial antenna designs

Table 4 shows the initial design parameters for the three antennas at the 400, 750, and 1000 MHz design frequencies. The three antennas were simulated in FEKO, and the results are discussed below. The axial mode input impedance for this class of antennas is expected to be stable over a bandwidth of approximately 40 - 60% [3], [31].

Figure 19 shows gain, VSWR, and input impedance results for the 400 MHz antenna. The simulated input impedance for the helical antenna is approximately flat around 200 Ω from ~270 to ~540 MHz. The flatness of the input impedance over the bandwidth of interest facilitates matching the antenna to a 50 Ω port using an impedance transformer. In this simulation, a reference impedance of 220 Ω is used as the feed impedance, without considering the impedance transformer. The 220 Ω is the natural input impedance of the helical antenna without any variation, which provides the best-case scenario for antenna bandwidth. Given these assumptions, the VSWR plot shows a bandwidth of 62%; the

simulated single element gain is around ten dBi, which agrees with the expected value based on the previously reported Applied Physical Electronics design [10].

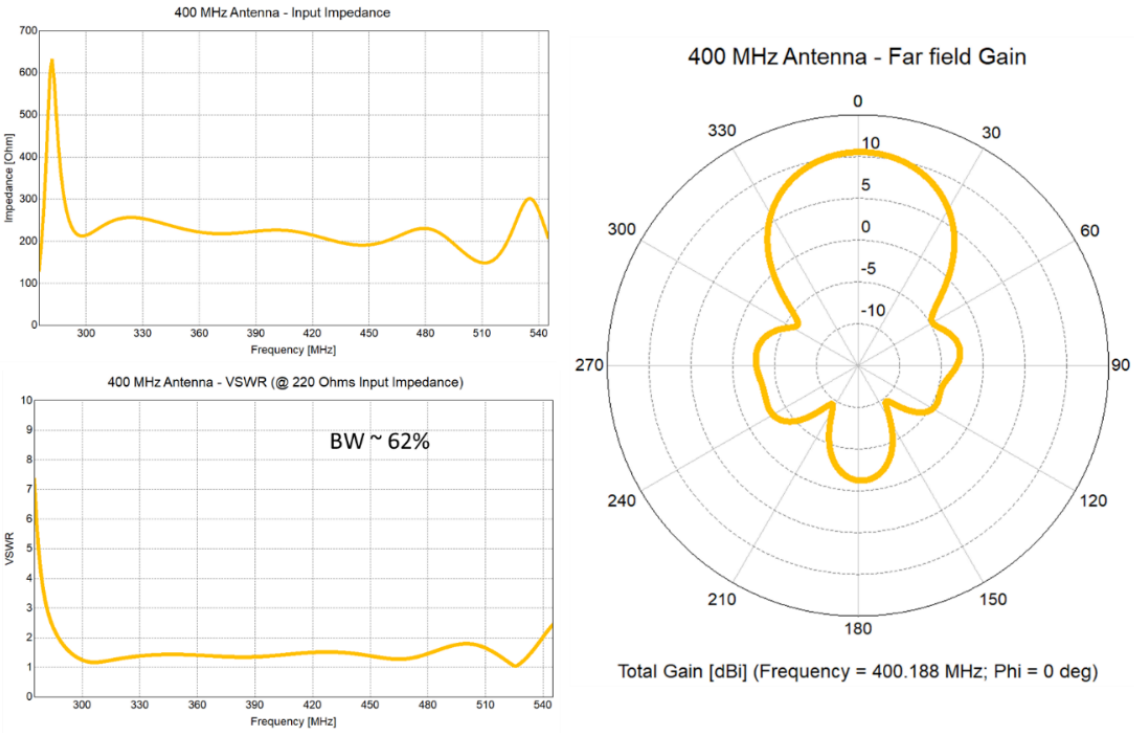

Figure 19. FEKO simulated 400 MHz Antenna referenced to $Z_{in} = 220\ \Omega$

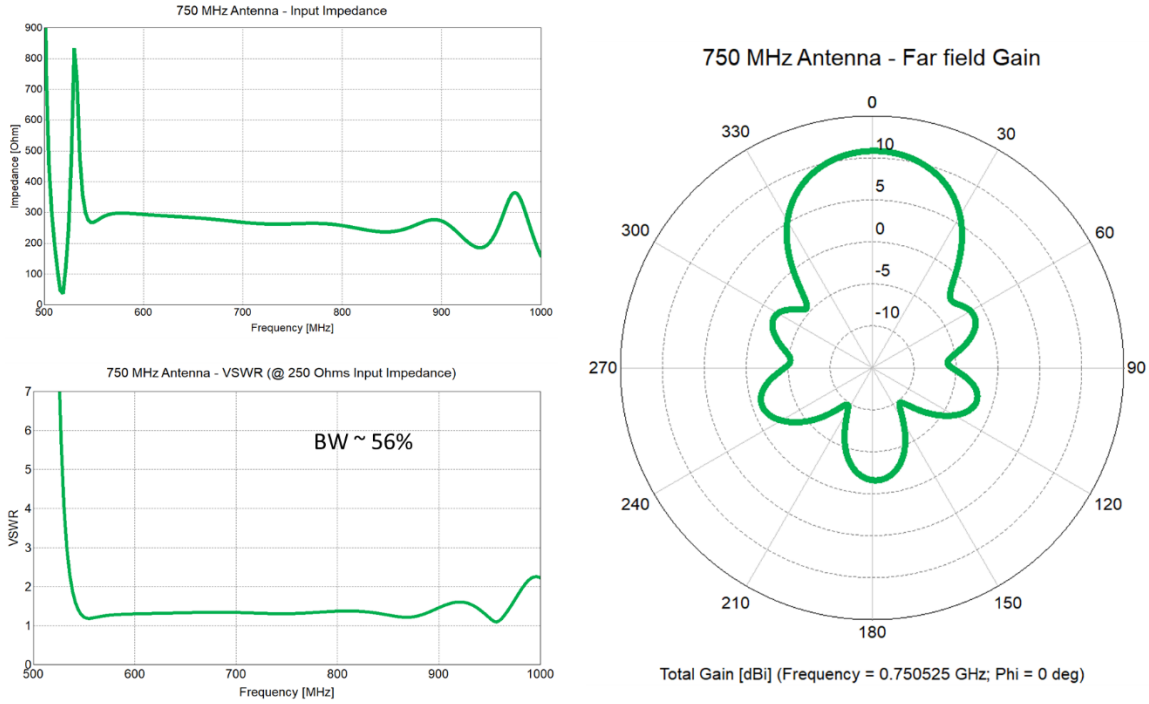

Figure 20. FEKO simulated 750 MHz antenna referenced to $Z_{in} = 250\ \Omega$

The 750 MHz design is shown in Figure 20 appears to have a higher-level input impedance over the desired bandwidth of around 200-300 Ω. The boresight gain at the design frequency appears to be higher at around 11 dBi. The ideal bandwidth for the antenna is found using a reference impedance of around 250 Ω, leading to a bandwidth of around 56%. For the input impedance vs. frequency plot, there seems to be a greater variation of the impedance across the bandwidth compared with the 400MHz antenna in Figure 19. Further, the impedance swing in the higher frequency band of both designs seems to be more exaggerated in Figure 20. The impedance behavior may be a function of frequency difference, or the number of turns, which is 6 for the 400 MHz antenna and 8 for the 750 MHz antenna.

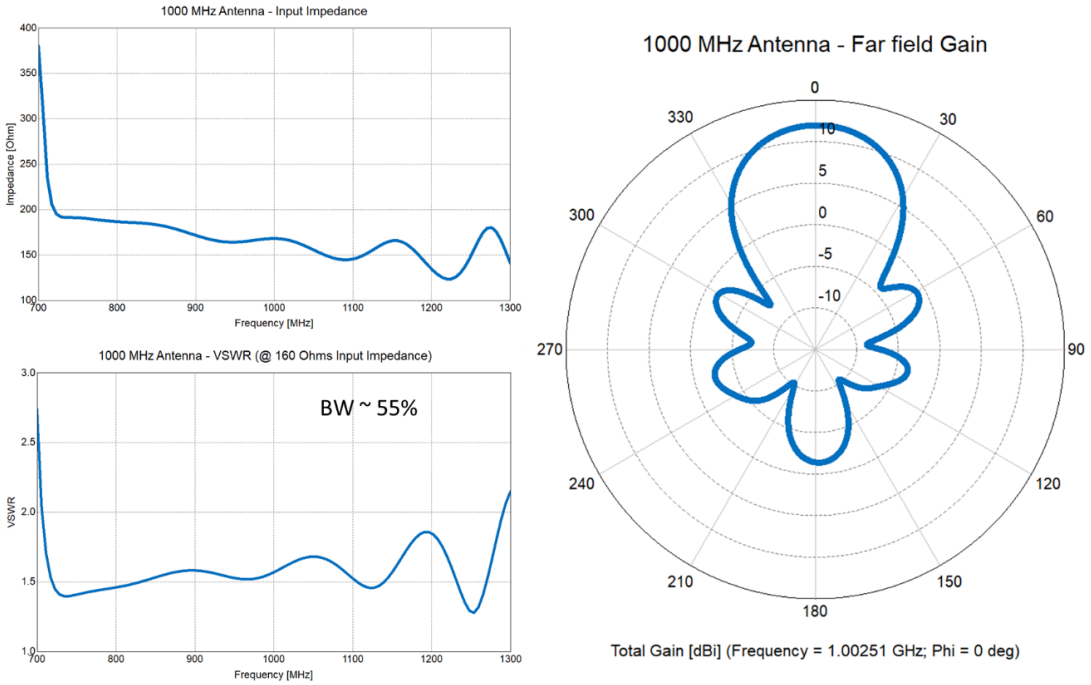

Figure 21. FEKO simulated 1000 MHz antenna referenced to $Z_{in} = 160\ \Omega$

Figure 21 shows the FEKO results for the 1 GHz design. The input impedance is significantly lower than the other two designs, the bandwidth referenced at 160 Ω is around 55%, and the gain exceeds 11 dBi.

Ground Plane Size

In EM simulation software such as CST and FEKO setting defined boundary conditions such as a Perfect Electric Conductor (PEC) can significantly speed up simulation and utilize less computational resources, the tradeoff is an alteration of the real-world model under simulation. Therefore, the parametric study would be much more convenient if an infinite ground plane (PEC boundary near the feed) is used instead of a defined ground plane diameter. Changes to the accuracy of the model due to the addition of an infinite ground plane can vary from slight to significant. So, we ran two simulations for the same model in FEKO to get a sense of the variability in the model's results. The model simulated is the 1000 MHz antenna mentioned earlier; the first simulation was ran using the dimensions shown in Table 4, and the second simulation used the same dimensions but with a finite circular ground plane with a diameter of 30 cm also assumed to be a PEC.

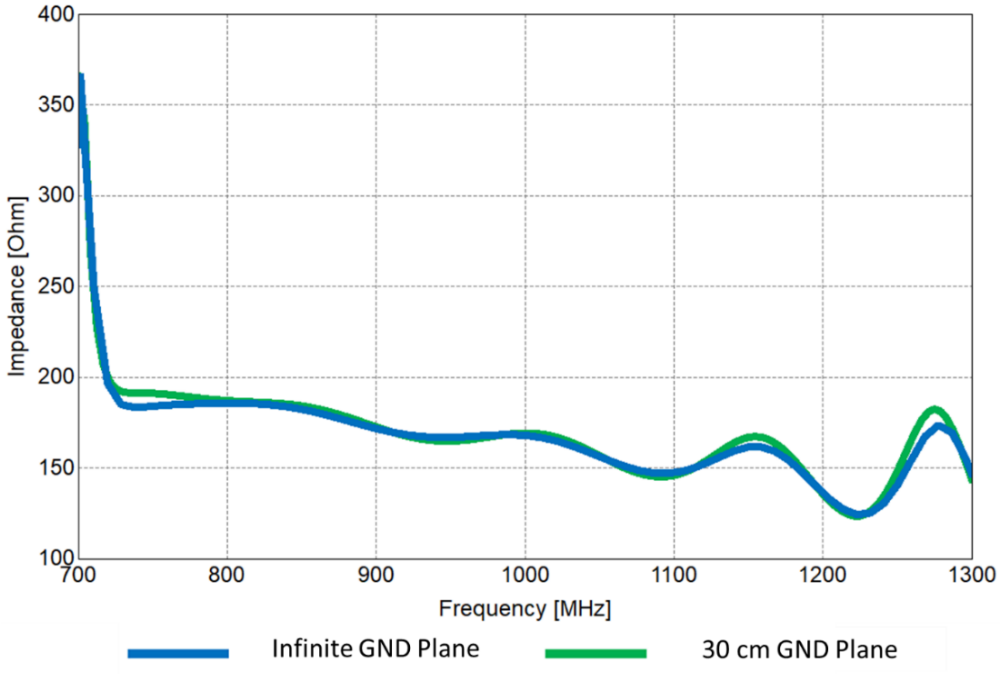

Figure 22. Input Impedance of a helical antenna above an infinite ground plane versus a finite GND Plane Size

Figure 22 compares the input impedance of the two models, the variation in input impedance for the 30 cm diameter GND plane vs. the infinite ground. Figure 22 shows that the finite ground plane exhibits insignificant differences from the finite ground plane over the bandwidth of operation.

Figure 23 compares the gain pattern of the same antenna design with the 30 cm GND diameter and the infinite ground. Based on the result, the gain seems to differ by one dBi between the two models.

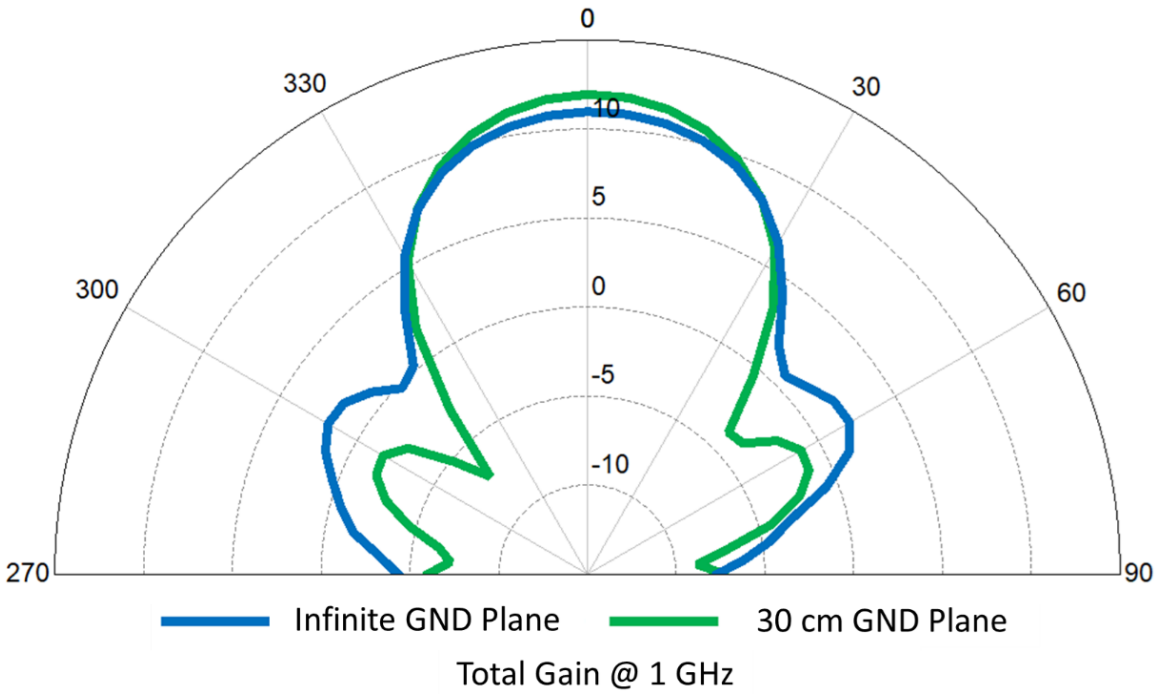

Figure 23. Gain VS. GND Plane Size

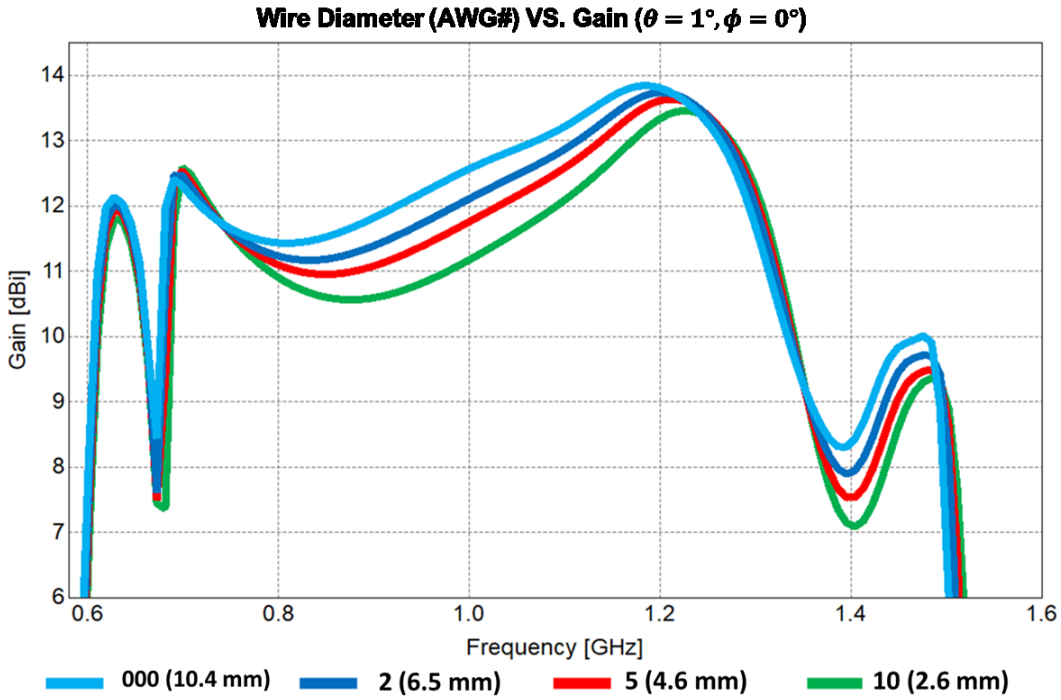

Figure 24. The Effect of wire diameter on the gain

It has been shown that increasing the conductor diameter increases the gain of the antenna at the operating frequency [42], [48]. In Figure 24, we vary the conductor diameter from 2.6 mm to 10.4 cm over 4 American Wire Gauge diameters [53]. Figure 23 shows that the gain of the antenna increases with the wire diameter. For the 1 GHz antenna with an infinite ground plane, the gain improves by 2.5 dBi as the wire diameter increases from 2.6 mm to 10.4 mm.

Another notable effect of changing the wire diameter is the variation in input impedance; changing the wire diameters can improve matching to the source. In [48], it is shown that matching to $50\ \Omega$ is possible when using a conductor diameter of 4.13 cm for a helical antenna working from 300 MH to 500 MHz. A FEKO simulation was done on the 1000

MHz antenna designed earlier in the chapter to find the input impedance variation with the wire diameter. Figure 25, the input impedance across frequency for three-wire diameters ranging from 2.6 mm to 10.4 mm. Going from 2.6mm to 10.4 mm reduces input impedance to between 80-100 Ω.

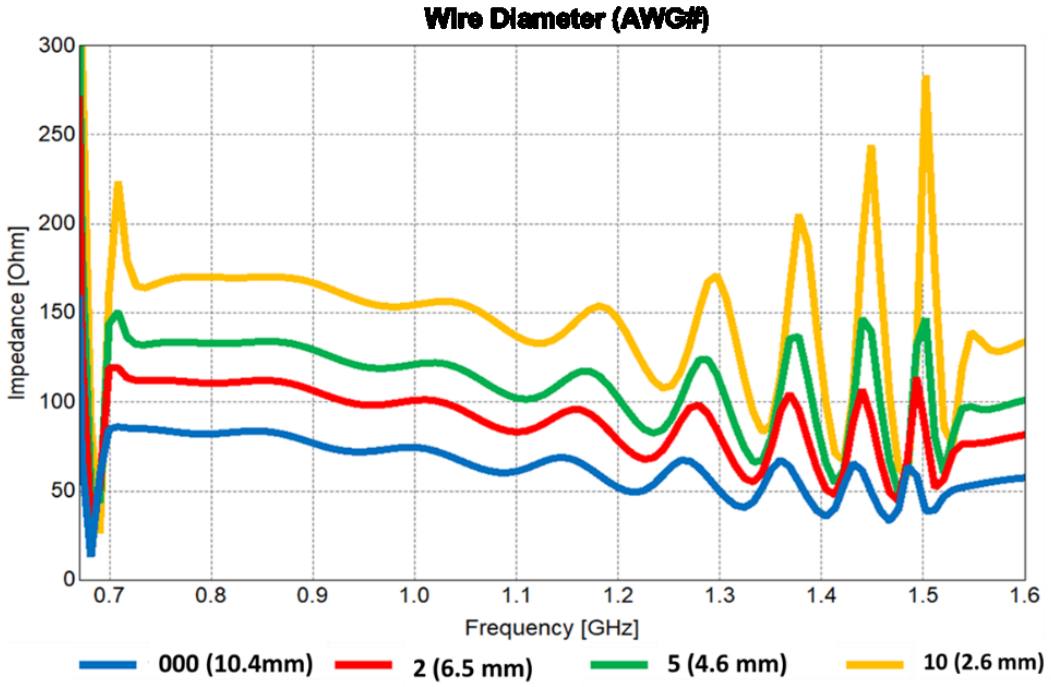

Figure 25. The Effect of wire diameter on the input impedance

Another advantage of using a thicker wire is reducing the impedance oscillations on the high end of the antenna bandwidth. If controller correctly, though, would allow for even further bandwidth in the axial and conical mode of antenna radiation. Where the bandwidth of the antenna can be extended up to 4 or 5 GHz leading to a 4:1 possible bandwidth ratio. Further increases in the wire diameter can further bring down the input impedance, while a 50 Ω input impedance is ideal, such impedance requires a 2 cm wide conductor. Such

diameters are not easy to fabricate as it introduces more mass which reduces flexibility, and it is not easy to interface to a standard coaxial connector.

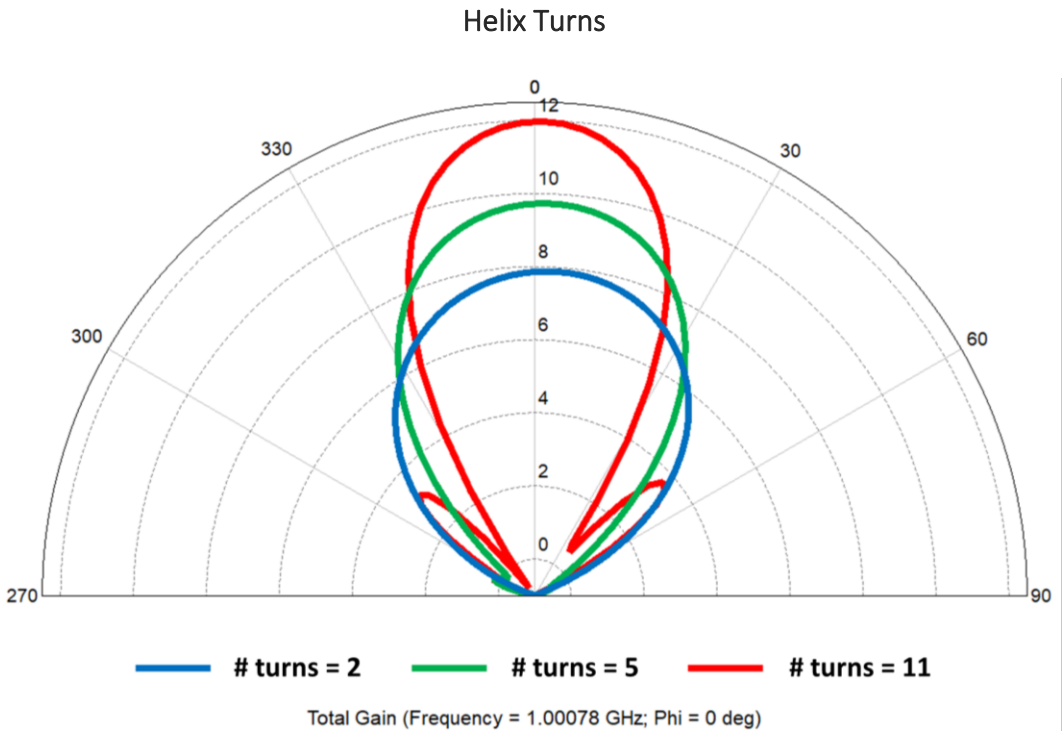

Figure 26. Number of Helix Turns vs. Far Field gain

Varying the number of turns for the boresight helical antenna translates into higher far-field gain, as shown in Figure 26. The antenna gain is around eight dBi for a helical antenna with two turns, ten dBi for the five turns helical, and 11 dBi for the nine turns helical antenna. The higher number of turns serves to focus the antenna Beamwidth in the far-field. A tradeoff in terms of gain is the higher introduced sidelobes on the antenna. For the two and five turns helical, the gain of side lobes is nonexistence above 0 dBi. While for the eleven turns, helical side-lobe gain can be around three dBi. Which is a drawback for the axial mode of operation since not all the energy is going in the boresight direction.

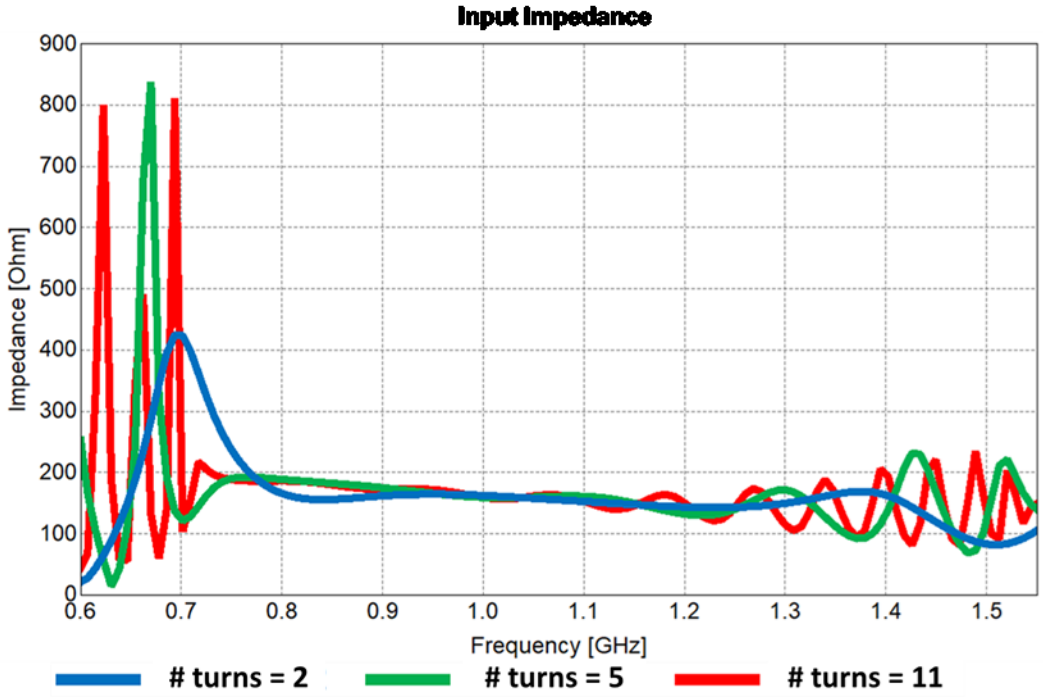

Figure 27. Input Impedance vs. Number of Turns

Other tradeoffs of the higher gain are large input impedance swings and deteriorated time-domain performance due to the increased signal travel distance in a dispersive medium. Figure 27 shows the input impedance for the three antennas with a different number of turns. An antenna with fewer turns exhibits a smoother input impedance curve, especially at the lower and upper ends of the antennas' bandwidth. Further, the flatness of the input impedance over the bandwidth is also affected as the blue plot seems to be the flattest of the three.

Next is the time-domain performance. A four and eight turn helical were simulated in CST Microwave Studio to characterize the time-domain performance deterioration due to the number of helix turns. The design parameters were kept the same as the 1 GHz antenna discussed earlier except for the number of turns and, by extension, the helix height. Both

structures were excited by an impeding plane wave in the azimuth direction ($e_i(t)$), which is equivalent to the field intensity due to the Tx antenna $e_{Tx}(t)$ as discussed in Chapter 2. The plane wave excitation is a modulated Gaussian pulse with spectral components covering the 1 GHz antenna operating bandwidth. The normalized pulse where the absolute peak value is 1, and its envelope are shown in Figure 28 (a). The received voltage at the antenna port ($u_{Rx}(t)$) is then measured, where the port is not being excited by a signal; instead, it is used to monitor the incoming plane wave. It follows that the voltage transfer function in Eq. 23 is the complete description of the simulated link in the time-domain.

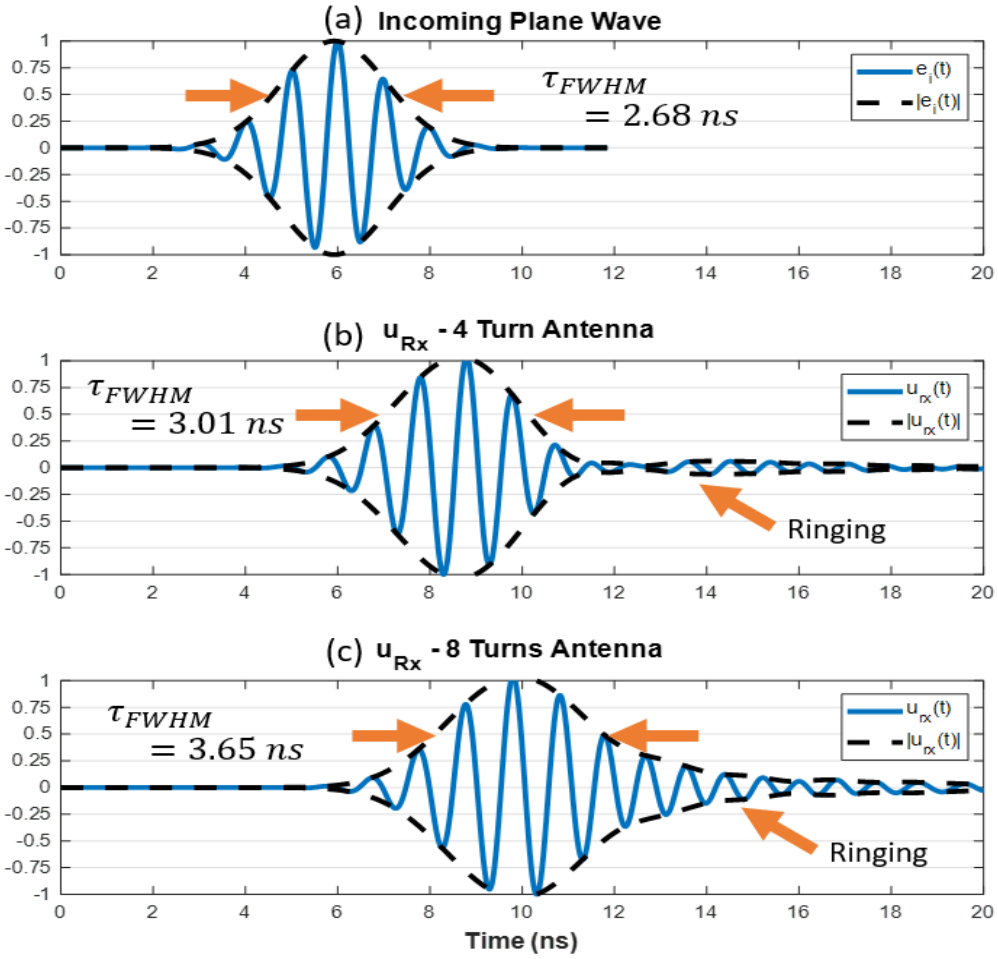

Figure 28. CST (a) Impeding wave, and received voltage at (b) 4 turn, and (c) 8 turn antennas

Here, we consider the ideal case, where only the Rx antenna is excited by a plane wave, meaning $\boldsymbol{r_{TxRx}}$ is large. Additional details can be found about the impulse response measurement and the analysis of transmitting and receiving modes in [47], [54]. From Figure 28, it is evident that the received normalized pulse at the 8-turn helical in Figure 28 (c) is more dispersed than that of the 4-turn helical in Figure 28 (b). The pulse received by the 8-turn helical antenna is around 20% wider than the 4-turn case, because $\tau_{FWHM}^{8TURN} = 3.65\, ns$ and $\tau_{FWHM}^{4TURN} = 3.01\, ns$.

As for ringing, the threshold α is chosen to be 0.2 of the peak value for the two antennas. To calculate ringing using Eq. 26 leads to $\tau_{r=.2}^{4TURN} = 4.53\, ns$, and for the 8 turn $\tau_{r=.2}^{8TURN} = 6.29\, ns$. The 8-turn antenna has 38% more ringing than the 4-turn helical, meaning dispersion and ringing are reduced in the antenna with fewer turns at the cost of gain. Since maintaining a low dispersion and achieving a high antenna gain are both critically favored in the final desired design, further investigation is needed to quantify how much dispersion can be tolerated or if gain can be reduced at the expense of lower signal dispersion, as will be addressed in the next chapter.

To access the suitability of an antenna for use with a specific short-pulse excitation the fidelity factor discussed is a useful parameter to check. The fidelity factor is an intuitive measure of the pulse, preserving the capacity of an antenna for a given pulse. In Figure 29 and Figure 30, we simulated antennas with three, eight, and eleven turns in FEKO and solved for the fidelity factors for the two example pulses discussed in Chapter 2. It is widely accepted that for UWB application, an antenna needs to have a fidelity factor of at least 0.9 to be considered operating.

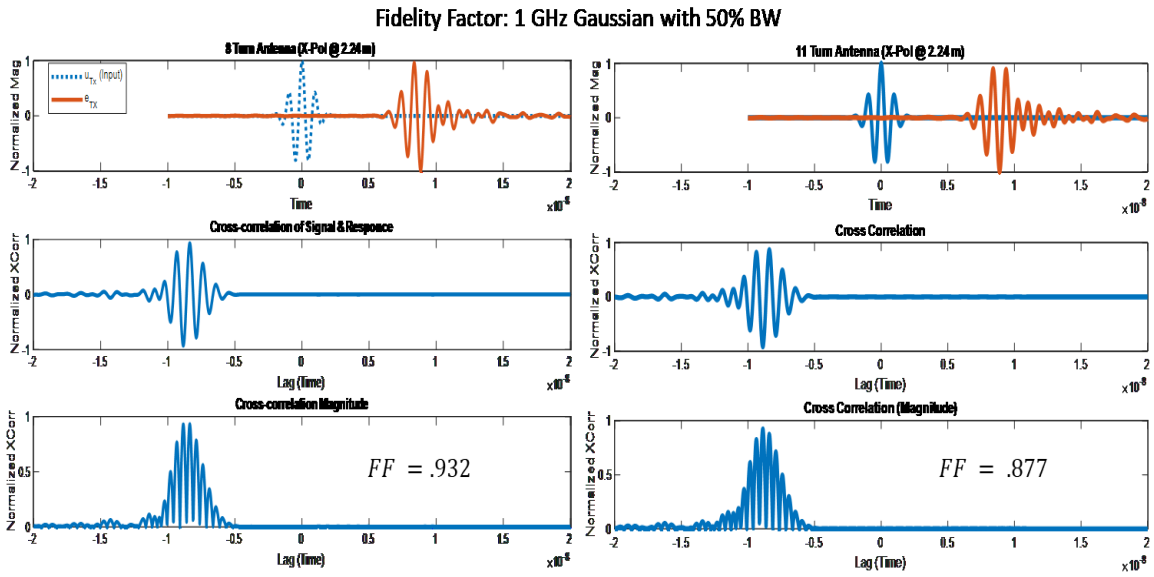

Figure 29. Helical FF for 1 GHz Gaussian with 50% BW

In Figure 29, a 1 GHz modulated Gaussian pulse with 50% is used to excite each of the two antennas in the transmitting configuration; the electrical field is then measured at a distance of 2.24 m away from the base of the antenna. Where the topmost subplot shows the excitation signal in blue and the normalized measured E field in orange. The middle subplot shows the normalize cross-correlation (autocorrelation) of the two signals and bottom subplot shows the calculated antenna fidelity factor. The antenna excited follows the same design discussed earlier, and the 50% bandwidth of the exciting signal is within the antenna's operating bandwidth.

For both the eight and eleven turn helical antennas, the orange pulse looks slightly different from the input pulse, with the field radiated from the eleven-turn antenna showing more variation. The difference between the measured fields and the input signal is quantified with a fidelity factor of .932 for the eight-turn antenna and .877 for the eleven-turn antenna. Therefore, the helical antenna with 11 turns is not suitable for short-pulse applications.

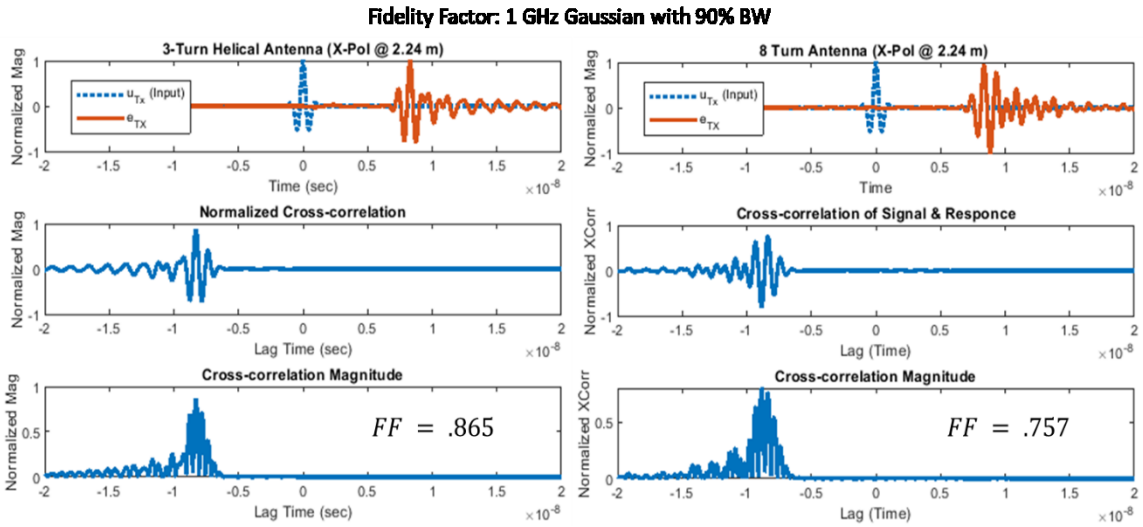

Figure 30. Helical FF for 1 GHz Gaussian with 90% BW.

To further extend the analysis, Figure 30 shows the fidelity factor derived from an input signal with a 90% bandwidth for three and eight turn helical antennas. The signal is highly deteriorated well below the accepted .9 FF, even for the three-turn helical antenna. The eight-turn helical antenna had a fidelity factor of .93 for the 50% Gaussian pulse. Here the same antenna has a fidelity factor of .76, as shown in the right plot in Figure 30. The reason is the signal spectral components lay outside of the 50-60% bandwidth range of the axial mode helical antenna mainly since the electric field value is recorded in the boresight direction. The frequencies beyond the bandwidth of the antenna are not radiated, distorting the radiated pulse.

Dielectric Rod

A support structure is typically necessary for the mechanical stability of helical antennas. A cheap and flexible support structure can be made by wrapping the helix around a 3D printed dielectric rod. A commonly used 3D printing filament is polylactic acid (PLA). If

the support has a permittivity constant higher than that of free space, adding the dielectric rod will shift the operating frequency of the antenna, and can affect its radiation performance. In this section, we discuss dielectric properties of PLA and conduct a parametric study on the effect of using a PLA dielectric as a support rod for the 1 GHz helical antenna previously described.

PLA Dielectric Properties

Fekicio *et al.* in [55] presented simulation and measurements of the complex permittivity of 3D printed PLA at the microwave range between 0.5 GHz and 20 GHz. The dielectric properties were measured indirectly using a microstrip line with stubs and a superstrate; a simulation sweep is then used to arrive at a complex permittivity value. Results from simulation and measurement show a dielectric constant of the printed material around 2.75 ± 0.05 and $\tan\delta = (1.1 \pm 0.2) \times 10^{-2}$ [55]. The mass density of PLA is around is quoted in the material database Matbase to have a range between $1210 - 1430 \frac{kg}{m^3}$ [56]. After investigating several commercial 3D printed PLA sources, it seems like the upper density range of $1430 \frac{kg}{m^3}$ is the most common [57].

Dielectric Thickness

Adding a PLA dielectric rod to the helix center affects the antenna performance in multiple ways. First, it shifts the bandwidth to lower frequencies, reduces gain, and increases the sidelobe levels due to the higher dielectric constant. The four different dielectric fill levels are used displayed in Figure 31, with

A- 9.24 cm diameter solid PLA Rod with a diameter of 9.24 cm

B- 9.24 cm diameter hallow PLA rod with a dielectric thickness of 1.677 cm

C- 9.24 cm diameter hallow PLA rod with a dielectric thickness of 0.770 cm

D- 9.24 cm diameter hallow PLA rod with a dielectric thickness of 0.213 cm

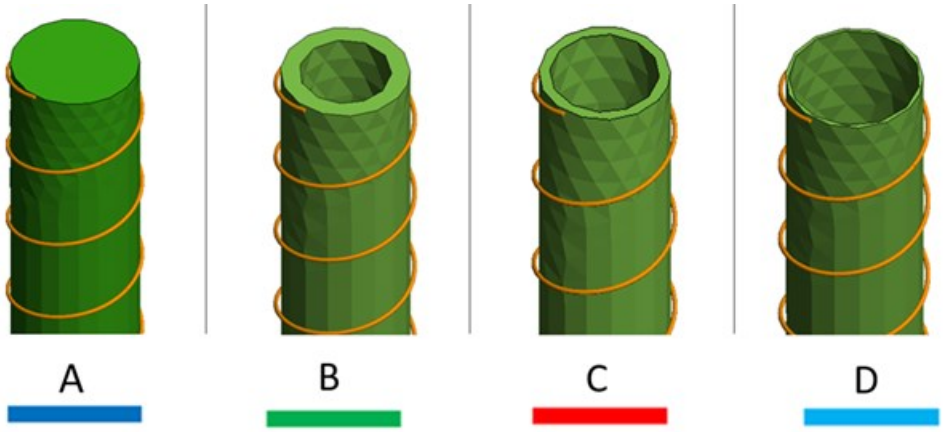

Figure 31. Dielectric Fill Level

A FEKO simulation was run to quantify the effect of dielectric thickness on the input reflection. Figure 32 shows a correlation between the dielectric thickness and the shift in VSWR. For example, rod C shows that adding the dielectric support makes the antenna unusable (VSWR > 2) for frequencies above 1.2 GHz. Which is a significant drawback; to get back the previous bandwidth, the size of the helix can be varied, which is what is discussed in the next section. The difference in the turn-on frequency between the most hallow rod (D) and the solid rod (A) is around 80 MHz. There is also a relation between the dielectric fill amount and the impedance swings in the upper antenna bandwidth. A solid rod seems to introduce significant impedance swings, as represented in the VSWR plot shown below. The hollow rods allow for much fewer impedance swings but are still notable.

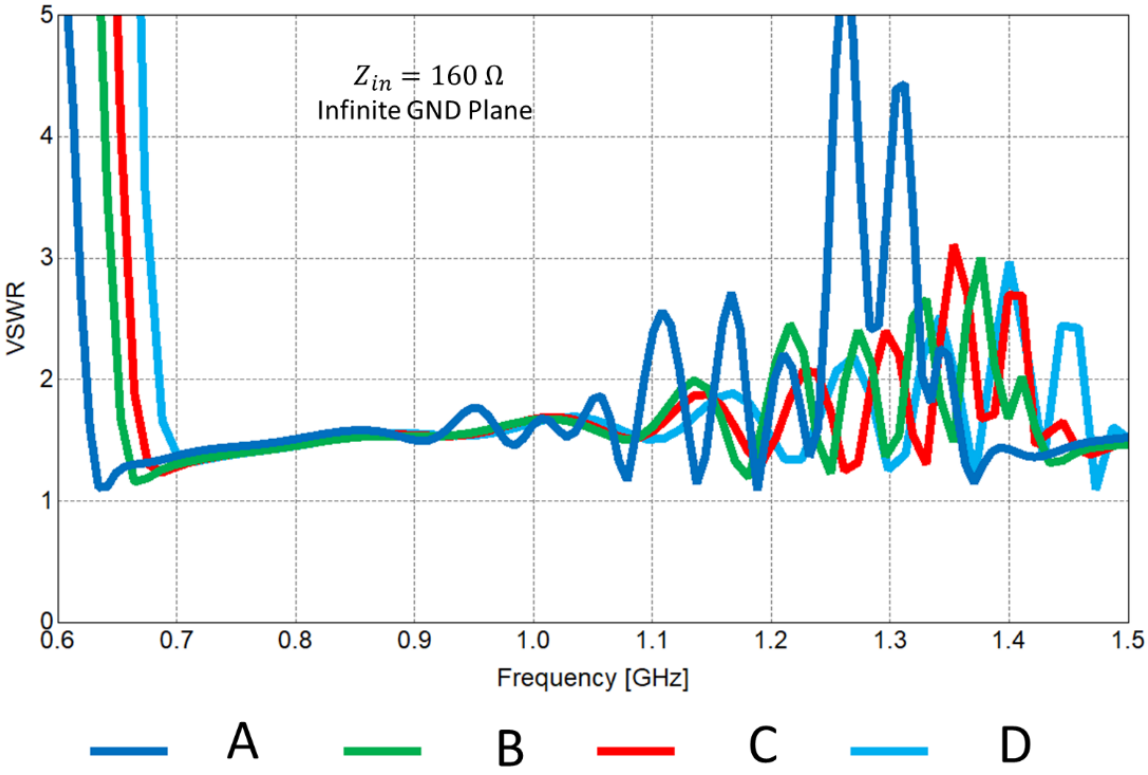

Figure 32. Frequency Shift vs. Dielectric Thickness

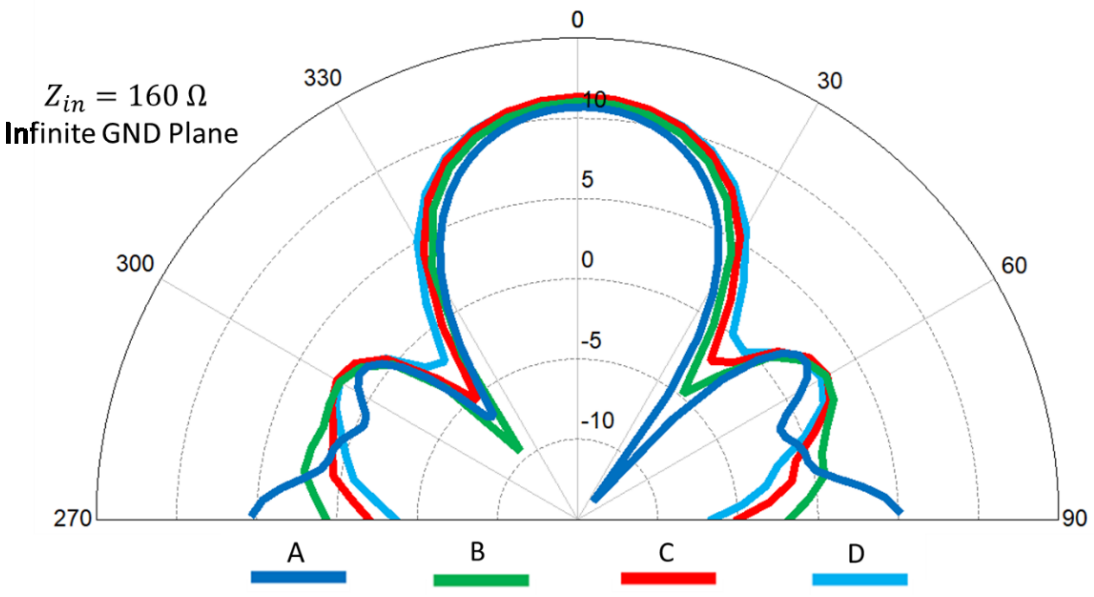

Figure 33. Gain vs. Dielectric Thickness

The presence of the rod also affects the far-field gain of the antennas. As shown in Figure 33, a higher fill slightly increases sidelobe levels, especially on the side in the axial mode of helical antenna operation. Having a higher fill also emphasizes the beam null around 45 degrees.

The third effect of the presence of the dielectric is the slightly less gain in the boresight of the antenna. The addition of the directrices seems to reduce the gain by around 2-3 dBi in the boresight direction. While lower axial mode gain is a drawback, the presence of a dielectric rod can support the shape and weight of the helix, therefore significantly simplifying fabrication.

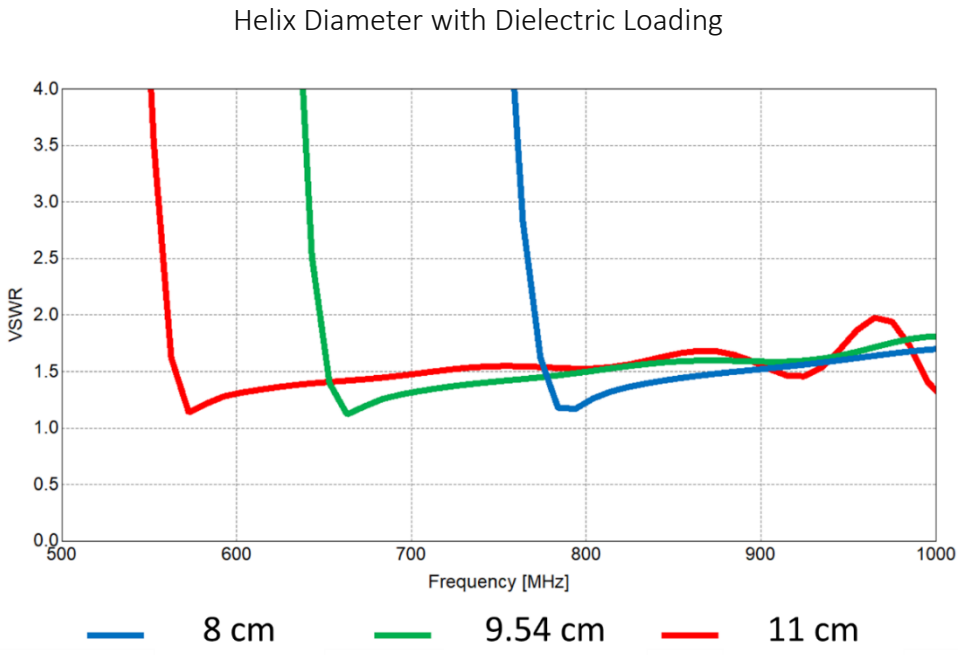

Figure 34. Frequency Shift vs. Dielectric Diameter

A FEKO parameter sweep was conducted to change the diameter of the antenna and dielectric to illustrate the effect of a bandwidth shift to compensate for the presence of the

PLA dielectric. This was done by using fill B from Figure 31 to change the diameter of the wire winding (helix diameter) and the dielectric rod while keeping the distance from the wire to the dielectric constant at 1.5 mm and the dielectric rod fill constant. Three helix diameters were simulated 8 cm, 9.24 cm, and 11 cm to see the effect on the input port's VSWR, as shown in Figure 34.

The original free space design radius was 9.54 cm when using the same radius with a PLA rod B; the turn-on frequency shifted to the left by around 30 MHz. It seems like the 8 cm antenna diameter in Figure 34 shifts the turn-on frequency to the right, and the 11 cm diameter further shifts the antenna turn on frequency to the left. To arrive at the design objective of covering the 1 GHz band symmetrical to a smaller helix diameter should be considered. The 8 cm diameter provides the closest result to the design objective and returns bandwidth to what it looked like before adding the dielectric, with the added advantage of mechanical support. In addition to the advantage of reducing the helix diameter by around 1 cm, which would be useful to minimize mutual coupling when this antenna is used in a larger array.

Impedance Matching

An Impedance mismatch at the input of an antenna causes reflections in the incident power. Therefore, even the best radiating element is useless without proper impedance matching to interface it to a source. A challenge with the helical antenna as the input impedance of an axial mode element is approximately a function of the circumference (C), and wavelength λ_0 at the design frequency f_0 [31], [42],

$$R \approx 140\left(\frac{C}{\lambda_0}\right) \qquad \text{Eq. 34}$$

The input impedance, R, is typically a real value in the range of $100 - 300\ \Omega$ depending on the frequency and geometry, which is a significant drawback that must be tackled in the design of the antenna. In this section, we discuss impedance matching theory and present multiple techniques for matching the impedance to a standard $50\ \Omega$. We then fabricate and measure an impedance transformer that works over the entire antenna bandwidth.

Matching Network Design

In general, it is always possible to design a matching network for any load, if Z_L has a positive real part. The input impedance of helical antennas can always be made approximately positive and real without a significant imaginary component by controlling length and phase of currents. The challenge becomes in finding the optimal impedance matching network based on several considerations such as complexity of the design, operating bandwidth, the medium of implementation (i.e., waveguide vs. PCB), and adjustability to post-fabrication tuning [2]. For example, an L network that uses lumped elements to achieve matching is too lossy and complex to cover the desired bandwidth. Frequency requirements would make it prohibitive for this application [2].

Quarter-Wave Transformer

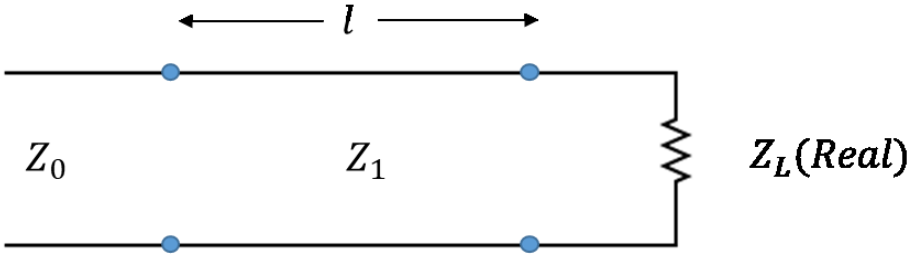

Figure 35. A quarter-wave matching transformer, when $\boldsymbol{l = \lambda_0/4}$ [2]

A quarter-wave transformer is a good place to start because it provides a narrowband impedance match and can be methodically extended to build wideband impedance matching devices. It can only be used to match to real loads, that being said, most loads can be adjusted to be real by with a specific length of a TL or by adding a reactive lumped component at the expense of loss or bandwidth as discussed above. An intuitive explanation of the operation of $\frac{\lambda}{4}$ the transformer is to compare the phases of the reflected singles from the Z_0, Z_1 and Z_1, Z_L junctions, it can be noticed that reflections from the second interface travel a distance of $\frac{\lambda}{2}$, thus adding destructively with the reflections from the first junction.

More rigorously, to find the characteristic impedance Z_1 of the single section quarter-wave transformer as shown in Figure 35, we assume R_L and Z_0 are real and known, and there is no reflection (Γ=0) in the case of a match. So, the input impedance looking into the Z_1 can be represented as,

$$Z_{in} = Z_1 \frac{R_L + jZ_1 \tan(\beta l)}{Z_1 + jR_L \tan(\beta l)} \qquad \text{Eq. 35}$$

Where is the phase constant or also called the wave number in a lossless medium is $\beta = \omega\sqrt{\mu\epsilon} = \frac{2\pi}{\lambda}$, and l is the distance from load looking into the matching network. For the equation above, $\beta l = \left(\frac{2\pi}{\lambda}\right)\left(\frac{\lambda}{4}\right) = \frac{\pi}{2}$, by substituting βl and simplifying Z_{in}, becomes $Z_{in} = \frac{Z_1^2}{R_L}$ By Setting $Z_1 = \sqrt{Z_0 R_L}$, the reflections from the load can be set to zero, but only at the single frequency that corresponds to λ_0. [2].

Small Reflections: Single Section

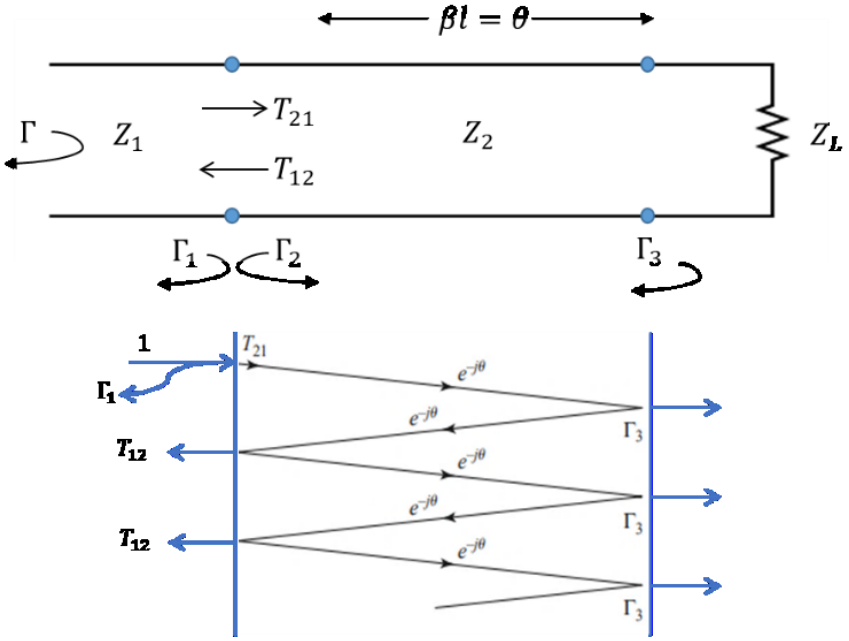

Figure 36. Partial reflections and transmissions in a single-section [2]

A general expression for the reflection coefficient when $\lambda \neq \lambda_0$ can be found using the small multi-reflections, as shown in Figure 36. Given $\Gamma_1 = \frac{Z_2 - Z_1}{Z_2 + Z_1}$, $\Gamma_2 = -\Gamma_1$, and $\Gamma_3 = \frac{Z_L - Z_2}{Z_L + Z_2}$, meaning $T_{21} = 1 + \Gamma_1 = \frac{2Z_2}{Z_1 + Z_2}$ and $T_{12} = 1 + \Gamma_2 = \frac{2Z_1}{Z_1 + Z_2}$. Extending this to an infinite sum of the small reflections for the single section gives the total reflection Γ as

$$\Gamma = \Gamma_1 + T_{12}T_{21}\Gamma_3 e^{-2\,j\theta} \sum_{n=0}^{\infty} \Gamma_2^n \Gamma_3^n e^{-2\,jn\theta} \qquad \text{Eq. 36}$$

The above is simplified as a converging geometric series into the form

$$\Gamma = \Gamma_1 + \frac{T_{12}T_{21}\Gamma_3 e^{-2j\theta}}{1 - \Gamma_2\Gamma_3 e^{-2\,jn\theta}} = \frac{\Gamma_1 + \Gamma_3 e^{-2j\theta}}{1 - \Gamma_1\Gamma_3 e^{-2\,jn\theta}} \qquad \text{Eq. 37}$$

This can be further simplified when the discontinuity between Z_1, Z_2 and Z_2, Z_L is small, so $|\Gamma_1\Gamma_3|$ is negligible. Therefore, the reflection can be approximated by using only the numerator as: $\Gamma = \Gamma_1 + \Gamma_3 e^{-2j\theta}$. Another way to say the same thing is that the total reflection is dominated by the first respective reflection of each section interface.

Small Reflections: Multi-Section

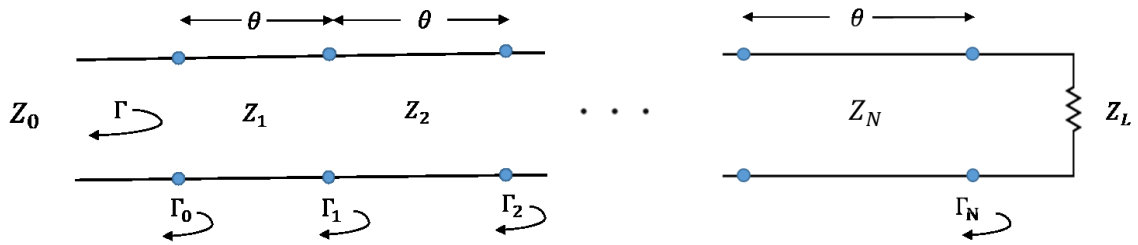

Figure 37. Partial reflections for a multi-section matching transformer [2]

The small reflections approximation can be extended to a multi-section transmission line with N equal-length sections, as shown in Figure 37. The total reflection coefficient by the small reflections of all the sections of a TL with monotonically varying impedance and a real load at the end is,

$$\Gamma(\theta) = \Gamma_0 + \Gamma_1 e^{-2\,j\theta} + \Gamma_2 e^{-4\,j\theta} + \cdots + \Gamma_N\, e^{-2\,j\,N\theta} \qquad \text{Eq. 38}$$

Using Eq. 33, a device with the desired reflection coefficient as a function of frequency (θ) can be synthesized by using enough sections (N). The challenge then becomes, what

number of sections, length, and bandwidth is good enough for the application [2]. Another problem specific to this project is the impact of a matching network on the time-domain response of the antenna.

Binomial and Klopfenstein Transformer Design

Table 5. 2D Binomial and Klopfenstein Transformers' Design Parameter

PARAMETER	BINOMIAL	KLOPFENSTEIN
f_{min}	800 MHz	800 MHz
R_L	160 Ω	160 Ω
ϵ_r	4.35	4.35
Transformer length	14.86 cm	11.76 cm
Input line Width	4.5 mm	2.9 mm
Output line Width	205.6 µm	130.5 µm
Substrate thickness	2.36 mm	1.5 mm
N	4	10

Table 6. Impedance Tapper Dimensions

There are many possible implantations for a multi-section transformer, below are Binomial and Klopfenstein implementations, they were selected due to their suitability to the application at hand. Two design validation prototypes for the 1 GHz band with the parameters in Table 6, were designed via Antenna Magus, then optimized in MATLAB and simulated in CST on FR4 substrate, fabrication is underway at UMKC.

The advantage of the binomial transform is the ability to provide a maximally flat response in over the working bandwidth starting from f_0, where ripples and impedance variations are minimized [2]. Figure 37 shows the simulated performance of the impedance

transformers described in Table 6 above. The flat and low Γ response is at the expense of bandwidth and length of transition, for example, the S_{11} the response shown in Figure 38, based on the parameters in Table 5, show that even though the Klopfenstein TL is shorter in length, it is still operational over a much wider bandwidth, with the disadvantage of high ripples and slightly degraded performance. On the other hand, the binomial transformer gives significantly better matching at f_0 compared to the Klopfenstein.

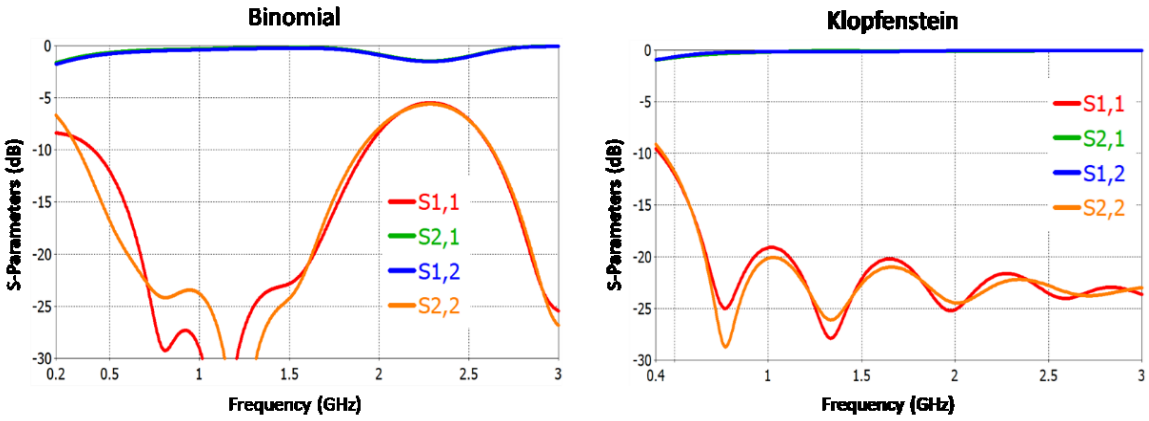

Figure 38. CST Performance of Klopfenstein and Binomial Transformers

For the helical antenna, the binomial transition may be sufficient in terms of bandwidth and impedance performance. The size and exciting waveform considerations can be limiting; that is, if there are frequency components of the exciting pulse outside of the matching bandwidth, it would be better to use the Klopfenstein transition. The main advantage of a Klopfenstein transition is the grantee of an optimal design That is, for a given length, the best match bandwidth is achieved, or alternatively, for a given bandwidth the shortest possible length of TL is achieved [43].

Klopfenstein Measurement

The Klopfenstein design was fabricated at UMKC using the LPKF S63 PB prototyping machine [58]. Figure 39 shows the VNA measurement setup used to compare the fabricated impedance tapper to the CST simulation of the model. In the simulation, both ports are terminated with $50\ \Omega$ loads, to compare quantitatively with the VNA's measurement given that the connectors used, and the VNA test cables all have a characteristic impedance of $50\ \Omega$. A Keysight eCal was used to calibrate the system, the IFBW used was 1 kHz, and the power level was set to 0 dBm.

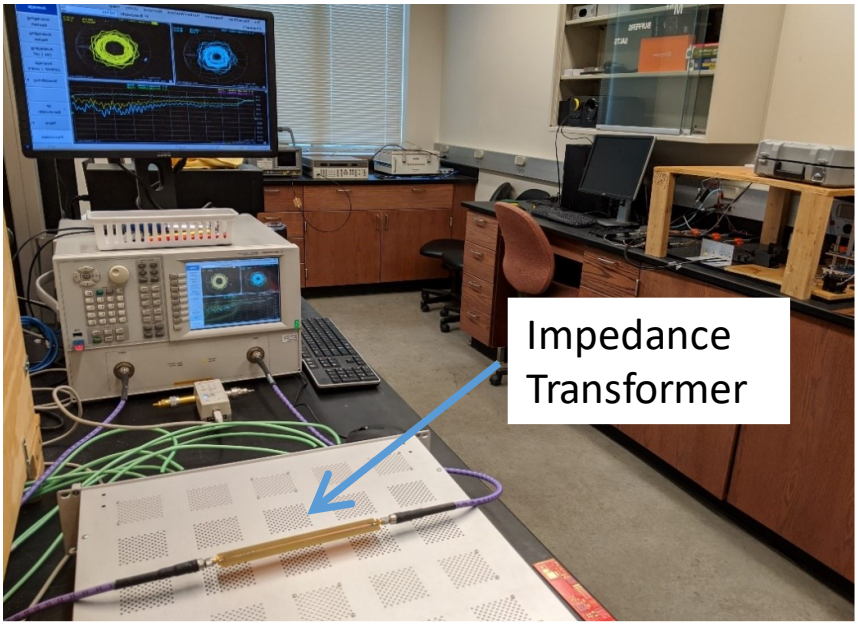

Figure 39.Impedance Transformer Measurement Setup

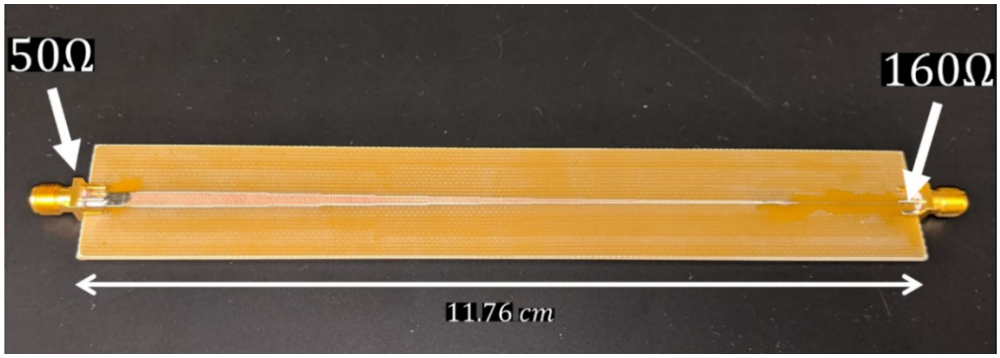

Figure 40.Klopfenstein Impedance Transformer on 1.5mm thick FR4

The reflection and transmission magnitude values are shown in Figure 41. The measurement is sufficient to show good agreement with the CST simulation as a validation to move forward with more complicated designs. Both the transmitted and reflected signals seem to match the expected simulation values within a few dB. Any slight mismatch can be due to reasonable loss and uncertainties in the form of dielectric uncertainty, soldering, connectors, and fabrication tolerance.

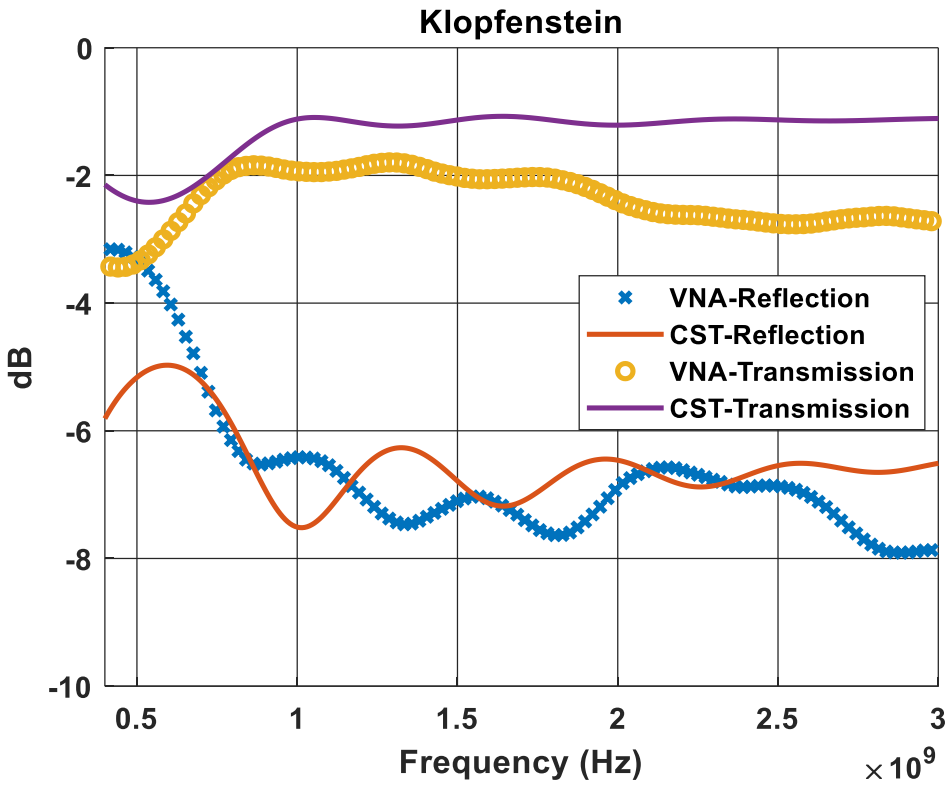

Figure 41.Simulation and $\mathbf{50\Omega}$ Reflection and Transmission Measurement

Figure 42 shows the CST simulated S11 response of the antenna with and without the addition of the impedance tapper. Adding the impedance tapper improves the input reflection from around -5 dB to -14 dB, meaning the antenna is operational after the addition of the impedance tapper. However, the results in Figure 41 were achieved using an

“equivalent network” analysis where the isolated impedance transformer was modeled as a network connected to the antenna, which was modeled by another equivalent network obtained from its isolated response. Future work will include simulating the entire setup, impedance transformer plus the antenna, in one full-wave simulation to investigate the effect of the presence of the impedance transformer on the performance of the antenna.

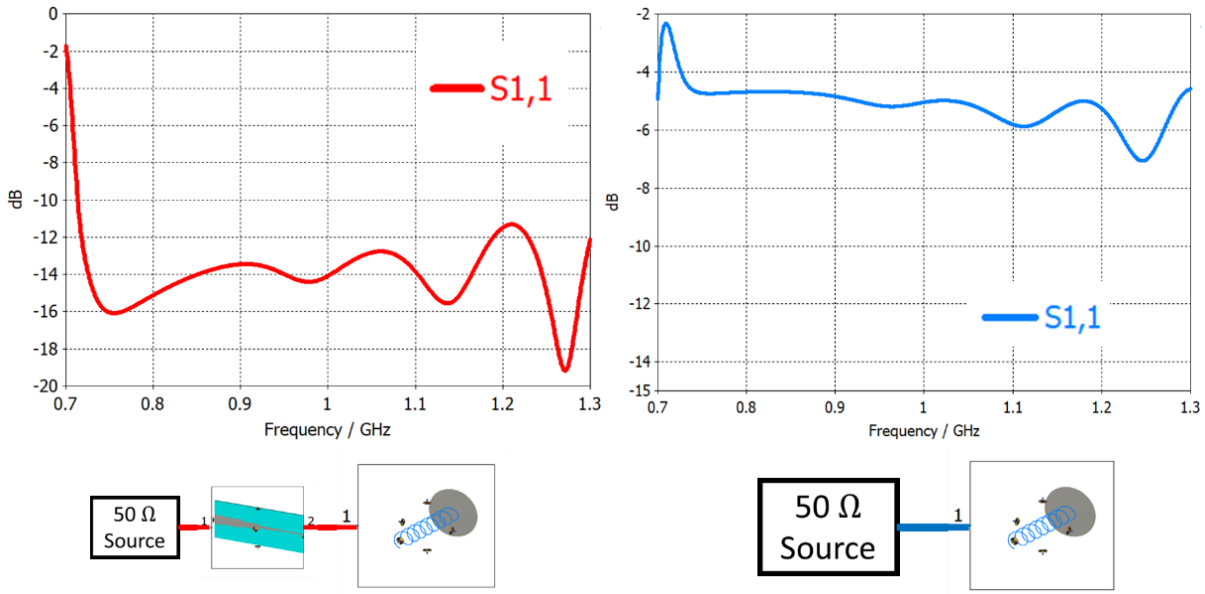

Figure 42. Antenna S11 with vs. without impedance tapper

Summary

In this chapter, we designed and simulated three antennas based on previously reported designs. The 1 GHz design presented here will be used for the optimization of antenna performance in the next chapter. Then conducted a parametric study of the many design parameters, listing the effect of varying each parameter on the design. The chapter ends with the design and measurement of wideband impedance transformers, followed by a CST simulation on the impact of the fabricated design on the 1 GHz designed antenna.

CHAPTER 6

HELICAL ANTENNA OPTIMIZATION

In this chapter a manual and iterative optimization based on the parametric analysis detailed in Chapter 5 is attempted to design a helical antenna for short-pulse applications. The design objectives are to maximize gain, minimize antenna size, improve time-domain performance for short-pulse applications, large bandwidth, and a flat input impedance as close to 50 Ω as possible. As discussed in Chapter 5, some of these requirements are direct contradictions of one another. For helical antennas, both high gain and small size or high gain and good time-domain behavior are inversely related. Therefore, optimization is needed to arrive at an acceptable design to address the competing requirements.

Antenna Optimization

PARAMETER	PROPOSED
Number of Turns (N)	4
Wire Diameter (d)	**6.54 mm (AWG#2)**
Ground Plane Diameter (Dg)	300 mm
Helix Diameter (D)	**95.43 mm**
Feed Height (Hf)	9.82 mm
Pitch Angle (α)	**17°**
Feed Pitch Angle	6.5°
Sense	**Right Handed**

(a)

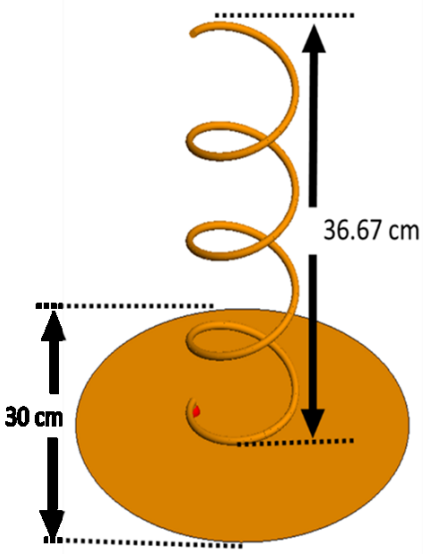

(b)

Figure 43. (a) Design Parameters (b) 3D model for the proposed antenna

In this section, we present an optimized helical antenna matching the criteria discussed above based on the literature review in Chapter 4 and the parameters discussed in Chapter 5. After several design iterations by tweaking designs presented in the literature and through a trial and error approach, the best design parameters reached are shown as the proposed design in Figure 43.

For far-field gain, a higher number of helix turns increases gain, so does a thicker wire diameter and a sharper pitch angle. There is a tradeoff between all of these factors and the input impedance. The tradeoff is in the form of level, flatness, ripples, and value of input impedance, in addition to the bandwidth of operation of the antenna.

- Increasing the number of turns is the most obvious way to boost far-field gain but comes at the cost of increased side lobes.
- Increasing the number of turns increases both the level, ripples and flatness of the input impedance
- A thicker wire typically reduces the input impedance up to a point, beyond which a thicker wire increases the input impedance. That point is dependent on the pitch angle of the antenna and can define the mode of the antenna radiation pattern in addition to the impedance.
- If the angles are limited to stay in the axial mode of radiation, then a thicker wire can reliably increase gain.
- When tuned carefully with other parameters, the sharper pitch angle, in conjunction with the appropriate wire diameter, can increase gain, reduce impedance swings, and even improve time-domain performance.

In the optimized design, we were able to improve the input impedance of the antenna in three ways, as shown in Figure 44; reduce the impedance ripples – which opened a much wider bandwidth for UWB signals, improve input impedance flatness, and reduced the impedance – which would make the design of an impedance matching section easier.

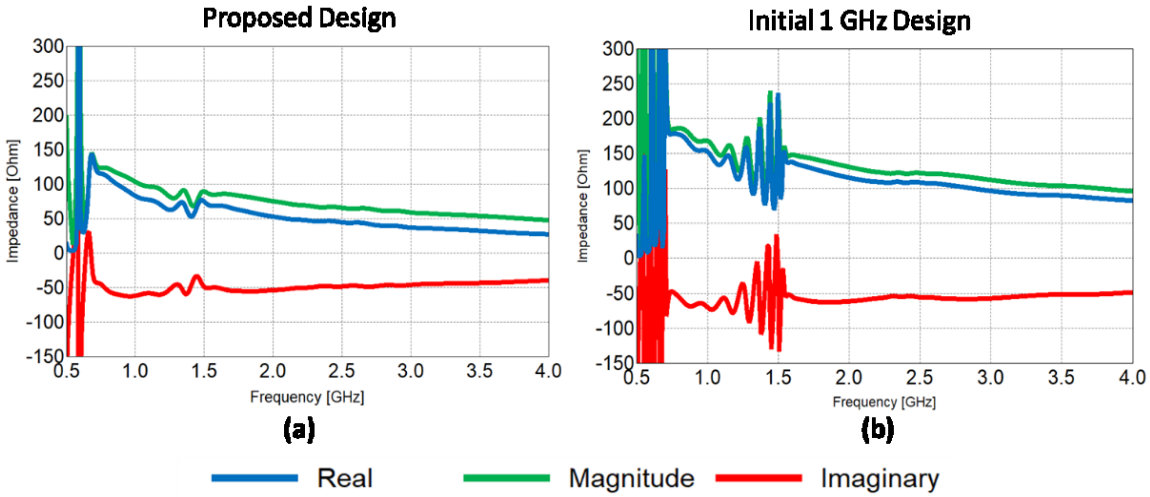

Figure 44. Input Impedance for initial 1 GHz design VS proposed design

The low and flat input impedance curve of the optimized antenna in Figure 44(a) is much better than the 1 GHz antenna design discussed in Chapter 4. The curve is flatter over a much larger operating bandwidth extending past 4 GHz. The removed ripples around the 1.5 GHz region reduce ringing at the input port and allow for the waveform preservation of UWB pulses that are significantly shorter or occupy more bandwidth than the previous design. The improved input impedance is due in part to the low feeding height of 9.8 mm and the use of two different pitch angles. One for the first half helical turn, the feed pitch angle of 6.5 degrees, in addition to a helix pitch angle of 17 degrees for the rest of the antenna. The combination of the wire diameter and smooth helical growth defined by the feed angle served to reduce the input impedance. That in addition to the combination of a thicker

AWG#2 wire, steeper pitch angle, and fewer number of turns served to reduce the impedance swings and improve flatness significantly.

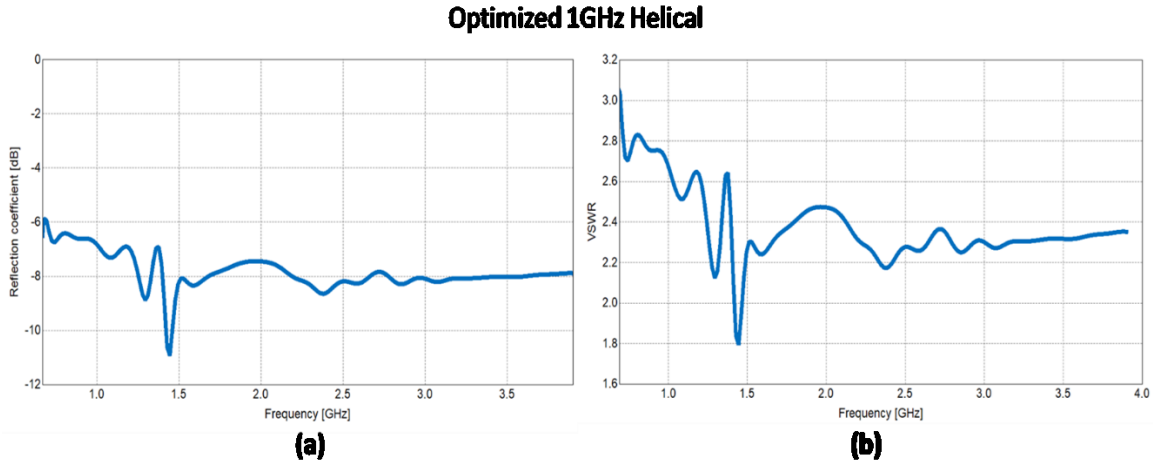

Figure 45. (a) S11 and (b)VSWR for the proposed antenna

Figure 45 shows the reflection from the input port of the antenna for a standard 50-ohm feeding. The VSWR is consistently less than 3 starting around 500 MHz well through 4 GHz. The VSWR and S11 shown in the plots above are without the use of any impedance tapper, which is a significant improvement from the design presented in Chapter 5. The input matching can be further improved using an impedance transformer similar to the one fabricated in Chapter 5.

The boresight antenna gain of the proposed design is displayed in Figure 46 (a), the gain pattern is as high at 12.6 dBi at 1.3 GHz. The gain is consistently above 9 dBi over the axial mode bandwidth. The gain rapidly drops off beyond 1.5 GHz due to beam spiting – that is, the transition to the conical mode of helical radiation. In the conical mode, the major lobe is split into two side lobes that eventually transition to the normal mode at much higher frequencies.

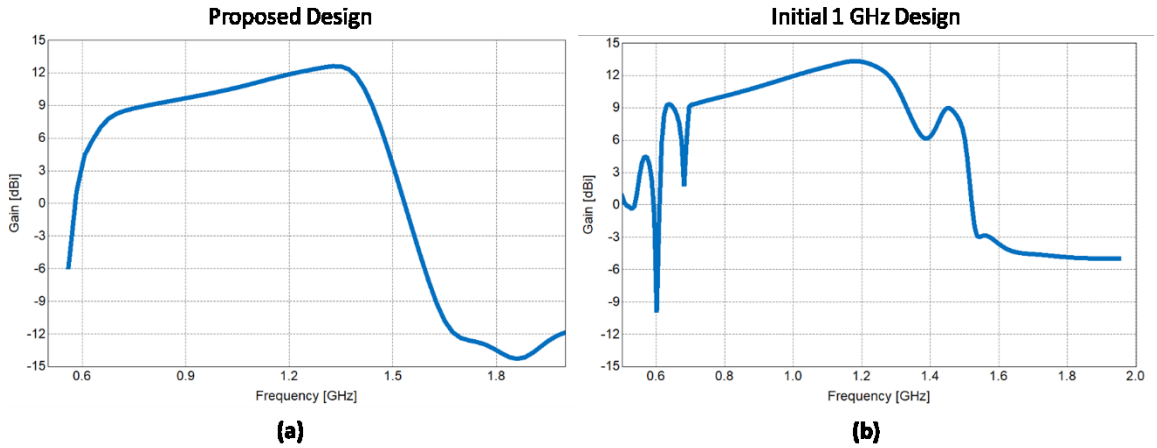

Figure 46. boresight gain for (a) proposed antenna (b) initial design

The proposed antenna gain vs. frequency is both smoother and flatter than the initial 1 GHz design based on the applied physical electronics design [10]. The plot in Figure 46 (b) has a significant gain variation between 600 and 700 MHz, then again near 1.4 GHz. The significant variation of gain is harmful in UWB systems, where the signal can occupy the entire bandwidth for two reasons. First, the gain swings affect the flatness of the antenna transfer function leading to reduced pulse preservation, and second, it is harder to use the antenna in an array for UWB when the gain pattern varies with frequency. Another notable advantage of the optimized design is the comparable gain between the two, even when the initial design used eight turns, and the proposed design uses four turns. Thus, significantly reducing element size, impedance ripples, and dispersion.

Another primary requirement for use in UWB applications is the optimized antenna must have a fidelity factor of more than .9, and preferably as close to 1 as possible while maintaining high gain in the boresight direction. Other time-domain priorities include low dispersion and minimal ringing. Acceptable dispersion is characterized by the minimum

stretching of the pulse by the antenna and measured by a minimized FWHM value. Based on the many parametric studies conducted in Chapter 5, the time-domain factors of the helical antenna can be improved by

- Reducing the antenna's physical size – with the number of helix turns being the most sensitive factor
- Dielectric rod medium – the presence of a dielectric rod other than free space significantly reduces short-pulse performance. This is due to the losses of the dielectric as represented by the value of the loss tangent of the dielectric medium and the ability of a dielectric to store energy as represented by the complex dielectric component of the dielectric constant of the medium.
- Antenna simulation in free space provided the best time-domain performance compared to several commercially available dielectric materials simulated
- Width of the conductor and growth angles – the geometry of the conductor and interactions of the signal with the ground plane significantly impacts the phase of the signal at the different signal frequency components. Therefore, as discussed in Chapter 2, the time-domain behavior can vary significantly due to group delay differences.
- Increasing the antenna bandwidth by ensuring robust and level input impedance over a broader frequency range that what is needed for the signal improves the fidelity factor of the transmitted field.

The proposed antenna design has excellent pulse preserving properties in the time-domain, even while maintaining high boresight gain discussed above. Figure 47 shows the

antenna fidelity factor for the same two gaussian pulses presented in Chapter 2 and used in Chapter 5.

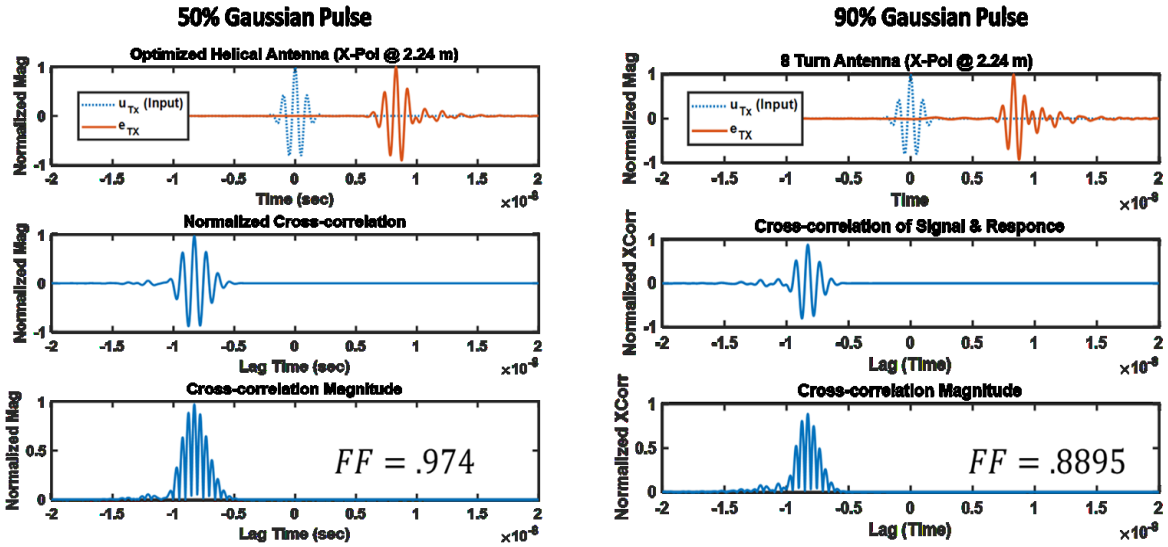

Figure 47. FF for the proposed antenna

In Figure 47, the topmost subplot shows the excitation signal in blue and the normalized measured E field in orange. The middle subplot shows the normalize cross-correlation (autocorrelation) of the two signals and bottom subplot shows the calculated antenna fidelity factor. For the 50% BW gaussian signal discussed earlier in this thesis, the proposed antenna provides a fidelity factor of .97 in the boresight direction at a distance of 2.24 meters away, that is, the antenna preserves 97 % of the pulse shape. The proposed antenna's FF exceeds the best simulated FF in Chapter 5, which was for the three turns free space helical with an FF of .95 for the 50% BW pulse at a distance of 2.24 meters. Another notable advantage of the proposed design is the surprisingly impressive performance, even for the 90% BW signal. The frequency components of a 1GHz signal with 90% BW lie outside of antenna bandwidth and even outside of a boresight gain pattern at those frequencies.

Nonetheless, the FF of the field at a distance of 2.24 meters is .8895, a smidge away from being operational for the UWB signal – this is the highest FF achieved for any antenna encountered in the preparation of this thesis for the 90% BW signal.

The size of the antenna is also greatly reduced compared to the 8-turn helical antenna presented in Chapter 5. The size of the initial 1 GHz design is around 50.9 liters, including the ground plane. The proposed antennas size is 33 liters including the ground plane. That is around 35% smaller footprint even with comparable gain, better impedance specs, and improved time-domain response.

Summary

In this chapter, we presented a manual iterative design of a UWB antenna to satisfy multiple competing design objectives. The optimized antenna has superb time-domain performance that is even better than a three-turn helical (.95 vs. .97) and better performance with the 90% BW Gaussian pulse than any other antenna simulated. The proposed design has excellent gain, nearly as good as the eight turns helical. The gain pattern is robust over the boresight mode over a broader frequency band and is much smoother. Slight sidelobes are introduced to the radiation pattern. The proposed design also has an excellent size compared to other helical antennas. The only limitation of this design being a perfect antenna is the mediocre input impedance matching to 50 ohms. The silver lining is the exceptionally flat impedance response over a meaningful bandwidth – in terms of the antenna mode. The fact that this antenna does not use a tapper means that it can be easily improved with an external tapper, or a tapper structure can be incorporate into the feed.

CHAPTER 7
CONCLUSION AND FUTURE WORK

In this thesis, the planar log-periodic and helix antennas were designed and numerically studied as two types of UWB antennas. The log-periodic had the advantage of frequency independence, therefore operating over a substantial bandwidth with excellent consistency in radiation properties. The disadvantage of the planar log-periodic was its distortion of short-pulse waveforms, as characterized by a low fidelity factor, rendering it useless for some short-pulse applications where the shape of the pulse must be preserved.

The helical antenna had several favorable characteristics such as tunable gain, better time-domain performance, and elliptical polarization that were explored in detail through several parametric studies. The drawback to the helical antenna was its narrower bandwidth; therefore, multiple antennas may be needed to cover the same bandwidth that a single log-periodic antenna can cover. The helical antenna is flexible, lending itself readily to optimizations to achieve the desired performance. A highly optimized design may improve some of the inherent limitations of the helical antenna.

We attempted to improve the size, fidelity factor, boresight gain, and input impedance first though manual iterative design. The optimized design maintained high gain and improved time-domain performance for UWB pulses while reducing antenna size, and input impedance.

Future work will include fabrication and experimental characterization of the optimized helical antenna for gain, efficiency, and time-domain performance in short-pulse

applications. For the experimental characterization of the antenna, a GTEM cell can be used for time-domain measurement as a novel method to characterize the antenna's response [47]. That is, the GTEM can excite a plane wave with a UWB pulse that can be measured at the antennas port to derive the impulse response. Having the measured impulse response or transfer function of the antenna would be used to verify the helical antenna's time-domain characteristics such as ringing, peak pulse value, width at half maximum, and fidelity factor; thus fully relating the numerical and experimental characterization of the antenna [5], [19].

Since the fidelity factor depends both on the antenna response and the exciting signal, numerical analysis of more application-specific pulses would be an excellent extension to work presented here. Another area of improvement would be to incorporate an impedance transformer into the structure of the antenna or its feed instead of a standalone design like what was done in Chapter 5. Further improvements to the proposed helical design would be to combine multiple helical antennas in parallel to bring down the input impedance further and significantly extend the bandwidth of a single element [37].

Finally, a multivariable optimization such as the Genetic Algorithm, can be used with custom fitness, and goal functions to automate the optimization of helical antennas designed in this work. Such an optimization can be implemented in FEKO via a Lua script or the command-line interface.

REFERENCES

[1] IEEE Standards Association, “145-2013 - IEEE standard for definitions of terms for antennas,” IEEE, New York, NY, 2013. doi: 10.1109/IEEESTD.2014.6758443.

[2] D. Pozar, *Microwave Engineering*, 4th ed. New Jersey: John Wiley & Sons, 2012.

[3] C. Balanis, *Antenna Theory: Analysis and Design*, 4th ed. New Jersey: John Wiley & Sons, 2016.

[4] R. Bansal, “The far-field: How far is far enough?,” *Appl. Microw. Wirel.*, vol. 11, no. 11, pp. 58–60, 1999, Accessed: Feb. 25, 2020. [Online]. Available: http://citeseerx.ist.psu.edu/viewdoc/summary?doi=10.1.1.186.2571.

[5] W. Wiesbeck, G. Adamiuk, and C. Sturm, “Basic properties and design principles of UWB antennas,” *Proc. IEEE*, vol. 97, no. 2, pp. 372–385, Feb. 2009, doi: 10.1109/JPROC.2008.2008838.

[6] D. Lamensdorf and L. Susman, “Baseband-pulse-antenna techniques,” *IEEE Antennas Propag. Mag.*, vol. 36, no. 1, pp. 20–30, Feb. 1994, doi: 10.1109/74.262629.

[7] D. M. Pozar, “Waveform Optimizations for Ultrawideband Radio Systems,” *IEEE Trans. Antennas Propag.*, vol. 51, no. 9, pp. 2335–2345, Sep. 2003, doi: 10.1109/TAP.2003.816313.

[8] X. Wang, A. Dinh, and D. Teng, “Radar Sensing Using Ultra Wideband – Design and Implementation,” in *Ultra Wideband - Current Status and Future Trends*, InTech, 2012.

[9] X. Liang, J. Deng, H. Zhang, and T. A. Gulliver, “Ultra-Wideband Impulse Radar Through-Wall Detection of Vital Signs,” *Sci. Rep.*, vol. 8, no. 1, p. 13367, Dec. 2018, doi:

10.1038/s41598-018-31669-y.

[10] M. B. Lara, M. G. Mayes, W. C. Nunnally, T. A. Holt, and J. R. Mayes, “Modular interchangeable high power helical antennas,” in *2011 IEEE Pulsed Power Conference*, Jun. 2011, pp. 358–363, doi: 10.1109/PPC.2011.6191444.

[11] J. R. Mayes, M. G. Mayes, W. C. Nunnally, and C. W. Hatfield, “Helical antennas for high powered RF,” in *2009 IEEE Pulsed Power Conference*, Jun. 2009, pp. 484–488, doi: 10.1109/PPC.2009.5386324.

[12] S. K. Singh *et al.*, “A high power UWB system with subnanosecond rise time using balanced TEM horn antenna,” in *2014 IEEE International Power Modulator and High Voltage Conference (IPMHVC)*, Jun. 2014, pp. 271–274, doi: 10.1109/IPMHVC.2014.7287261.

[13] B. Cadilhon, B. Cassany, P. Modin, J.-C. Diot, V. Bertrand, and L. Pecastaing, “Ultra wideband antennas for high pulsed power applications,” in *Ultra Wideband Communications: Novel Trends - Antennas and Propagation*, InTech, 2011.

[14] C. E. Baum and E. G. Farr, “Impulse radiating antennas,” in *Ultra-Wideband, Short-Pulse Electromagnetics*, 1st ed., Boston, MA: Springer International Publishing, 1993, pp. 139–147.

[15] E. S. Ramon, J. S. Tyo, R. W. Ziolkowski, M. C. Skipper, M. D. Abdalla, and J. Martin, “Integration and operation of an electrically small magnetic EZ antenna with a high-power standing wave oscillator source,” *IEEE Antennas Wirel. Propag. Lett.*, vol. 15, pp. 642–645, 2016, doi: 10.1109/LAWP.2015.2465869.

[16] A. Erentok and R. W. Ziolkowski, “Metamaterial-inspired efficient electrically small

antennas," *IEEE Trans. Antennas Propag.*, vol. 56, no. 3, pp. 691–707, Mar. 2008, doi: 10.1109/TAP.2008.916949.

[17] R. Li, B. Pan, J. Laskar, and M. M. Tentzeris, "A compact broadband planar antenna for GPS, DCS-1800, IMT-2000, and WLAN applications," *IEEE Antennas Wirel. Propag. Lett.*, vol. 6, pp. 25–27, 2007, doi: 10.1109/LAWP.2006.890754.

[18] T. Zwick, W. Wiesbeck, J. Timmermann, and G. Adamiuk, *Ultra-wideband RF system engineering*, vol. 9781107015. 2011.

[19] D.-H. Kwon, "Effect of Antenna Gain and Group Delay Variations on Pulse-Preserving Capabilities of Ultrawideband Antennas," *IEEE Trans. Antennas Propag.*, vol. 54, no. 8, pp. 2208–2215, Aug. 2006, doi: 10.1109/TAP.2006.879189.

[20] A. Smith, "Received Voltage Versus Antenna Height," *IEEE Trans. Electromagn. Compat.*, vol. EMC-11, no. 3, pp. 104–111, Aug. 1969, doi: 10.1109/TEMC.1969.302998.

[21] M. Koohestani, A. A. Moreira, and A. K. Skrivervik, "Fidelity concepts used in UWB systems," in *2014 IEEE Antennas and Propagation Society International Symposium (APSURSI)*, Jul. 2014, pp. 824–825, doi: 10.1109/APS.2014.6904740.

[22] H. Fallahi and Z. Atlasbaf, "Study of a class of UWB CPW-Fed monopole antenna with fractal elements," *IEEE Antennas Wirel. Propag. Lett.*, vol. 12, pp. 1484–1487, 2013, doi: 10.1109/LAWP.2013.2289868.

[23] R. Sammeta and D. S. Filipovic, "Quasi Frequency-Independent increased bandwidth planar Log-Periodic antenna," *IEEE Trans. Antennas Propag.*, vol. 62, no. 4, pp. 1937–1944, Apr. 2014, doi: 10.1109/TAP.2014.2302001.

[24] H. Nakano, “Frequency-Independent antennas: Spirals and Log-Periodics,” in *Modern Antenna Handbook*, Wiley, 2008, pp. 263–323.

[25] D. Isbell, “Log Periodic dipole arrays,” *IRE Trans. Antennas Propag.*, vol. 8, no. 3, pp. 260–267, May 1960, doi: 10.1109/TAP.1960.1144848.

[26] R. Sammeta and D. S. Filipovic, “Reduced size planar dual-polarized Log-Periodic antenna for bidirectional high power transmit and receive applications,” *IEEE Trans. Antennas Propag.*, vol. 62, no. 11, pp. 5453–5461, Nov. 2014, doi: 10.1109/TAP.2014.2352645.

[27] R. Sammeta, “Low-profile antennas for wideband transmit application in HF/UHF bands,” 2014, Accessed: Mar. 20, 2019. [Online]. Available: https://scholar.colorado.edu/ecen_gradetds/92.

[28] Altair Engineering, “FEKO.” Troy, Michigan, Mar. 1991, Accessed: Jun. 13, 2020. [Online]. Available: https://altairhyperworks.com/feko/.

[29] R. W. Ziolkowski and P. Jin, “Metamaterial-based dispersion engineering to achieve high fidelity output pulses from a Log-Periodic dipole array,” *IEEE Trans. Antennas Propag.*, vol. 56, no. 12, pp. 3619–3629, Dec. 2008, doi: 10.1109/TAP.2008.2007277.

[30] H. G. Schantz, “Dispersion and UWB antennas,” in *2004 International Workshop on Ultra Wideband Systems Joint with Conference on Ultra Wideband Systems and Technologies. Joint UWBST & IWUWBS 2004 (IEEE Cat. No.04EX812)*, 2004, no. May, pp. 161–165, doi: 10.1109/UWBST.2004.1320956.

[31] H. E. King, J. L. Wong, and E. H. Newman, “Helical antennas,” in *Antenna Engineering Handbook*, 4th ed., J. Volakis, Ed. New York, NY: McGraw-Hill Professional, 2007, pp.

1–26.

[32] K. Fujimoto, *Mobile Antenna Systems Handbook*. 2013.

[33] Z. Blazevic and M. Skiljo, “Helical Antennas in Satellite Radio Channel,” in *Advances in Satellite Communications*, InTech, 2011.

[34] I. V. Romanchenko *et al.*, “Four channel high power rf source with beam steering based on gyromagnetic nonlinear transmission lines,” *Rev. Sci. Instrum.*, vol. 88, no. 5, p. 054703, May 2017, doi: 10.1063/1.4983803.

[35] R. Kazemi, J. Palmer, F. Quaiyum, and A. E. Fathy, “Steerable miniaturised printed quadrifilar helical array antenna using digital phase shifters for BGAN/GPS applications,” *IET Microwaves, Antennas Propag.*, vol. 12, no. 7, pp. 1196–1204, Jun. 2018, doi: 10.1049/iet-map.2017.0959.

[36] I. V. Romanchenko, V. V. Rostov, A. V. Gunin, and V. Y. Konev, “High power microwave beam steering based on gyromagnetic nonlinear transmission lines,” *J. Appl. Phys.*, vol. 117, no. 21, p. 214907, Jun. 2015, doi: 10.1063/1.4922280.

[37] W. Coburn, “A numerical study of coaxial helical antennas,” in *Applied Computational Electromagnetics Society Journal*, 2010.

[38] S. I. H. Shah and S. Lim, “Bioinspired DNA Origami Quasi-Yagi Helical Antenna with Beam Direction and Beamwidth Switching Capability,” *Sci. Rep.*, vol. 9, no. 1, p. 14312, Dec. 2019, doi: 10.1038/s41598-019-50893-8.

[39] T. Topa, A. Noga, and A. Karwowski, “Adapting MoM with RWG basis functions to GPU technology using CUDA,” *IEEE Antennas Wirel. Propag. Lett.*, vol. 10, pp. 480–483, 2011, doi: 10.1109/LAWP.2011.2154373.

[40] Dassault Systèmes, “CST Studio Suite,” *2019*. https://www.3ds.com/products-services/simulia/products/cst-studio-suite/ (accessed Mar. 05, 2020).

[41] O. J. Glasser and J. D. Kraus, “Measured Impedances of Helical Beam Antennas,” *J. Appl. Phys.*, vol. 19, no. 2, pp. 193–197, Feb. 1948, doi: 10.1063/1.1698394.

[42] J. D. Kraus, “The Helical antenna,” *Proc. IRE*, vol. 37, no. 3, pp. 263–272, Mar. 1949, doi: 10.1109/JRPROC.1949.231279.

[43] R. Klopfenstein, “A Transmission Line taper of improved design,” *Proc. IRE*, vol. 44, no. 1, pp. 31–35, Jan. 1956, doi: 10.1109/JRPROC.1956.274847.

[44] R. Collin, “The Optimum Tapered Transmission Line Matching Section,” *Proc. IRE*, vol. 44, no. 4, pp. 539–548, Apr. 1956, doi: 10.1109/JRPROC.1956.274938.

[45] J. D. Kraus, “A 50-Ohm Input Impedance for Helical Beam Antennas,” *IEEE Trans. Antennas Propag.*, vol. 25, no. 6, p. 913, 1977, doi: 10.1109/TAP.1977.1141687.

[46] Shootthedevgru, “File:UHF CB with rubber ducky exposed,” *Wikimedia Commons*, 2008. https://en.wikipedia.org/wiki/File:UHF_CB_with_rubber_ducky_exposed.jpg (accessed May 10, 2020).

[47] S. Sczyslo, H. Thye, G. Armbrecht, S. Dortmund, and T. Kaiser, “Determination of the impulse response of UWB antennas using GTEM cells,” in *2009 IEEE International Conference on Ultra-Wideband*, Sep. 2009, pp. 753–758, doi: 10.1109/ICUWB.2009.5288800.

[48] D. V Giri and J. Levine, “The effect of minor radius on the performance of a Helical antenna,” Albuquerque, NM, 2016. Accessed: Mar. 29, 2020. [Online]. Available: http://ece-research.unm.edu/summa/notes/SSN/SSN577.pdf.

[49] M. Young, “Design and Testing of Helical Antennas for A RF Test Facility,” University of Missouri-Columbia, 2012.

[50] K. LaCalli, “Phased helical antenna array design for CubeSat application,” in *2018 IEEE Aerospace Conference*, Mar. 2018, vol. 2018-March, pp. 1–13, doi: 10.1109/AERO.2018.8396545.

[51] M. N. Hasan, O. J. Babarinde, S. Das, and K. V. Babu, “Dispersion Characterization of a UWB Vivaldi Antenna in Time and Frequency Domain,” in *2018 IEEE Indian Conference on Antennas and Propogation (InCAP)*, Dec. 2018, pp. 1–4, doi: 10.1109/INCAP.2018.8770763.

[52] C. Gouveia, C. Loss, P. Pinho, and J. Vieira, “Different Antenna Designs for Non-Contact Vital Signs Measurement: A Review,” *Electronics*, vol. 8, no. 11, p. 1294, Nov. 2019, doi: 10.3390/electronics8111294.

[53] “American Wire Gauge,” *Anixter*. https://www.anixter.com/en_us/resources/literature/wire-wisdom/american-wire-gauge.html (accessed Jun. 13, 2020).

[54] J. Kunisch, “Implications of Lorentz reciprocity for ultra-wideband antennas,” in *2007 IEEE International Conference on Ultra-Wideband*, Sep. 2007, pp. 214–219, doi: 10.1109/ICUWB.2007.4380944.

[55] J. M. Felício, C. A. Fernandes, and J. R. Costa, “Complex permittivity and anisotropy measurement of 3D-printed PLA at microwaves and millimeter-waves,” in *ICECom 2016 - Conference Proceedings, 22nd International Conference on Applied Electromagnetics and Communications*, Feb. 2017, doi:

10.1109/ICECom.2016.7843900.

[56] Idemat and Han Remmerswaal, “Material properties of Polylactic Acid (PLA),” *Matbase*, 1998. https://web.archive.org/web/20120210194852/http://www.matbase.com/material/polymers/agrobased/polylactic-acid-pla/properties (accessed Mar. 31, 2020).

[57] “What is the Density of PLA? - 3D Insider.” https://3dinsider.com/pla-density/ (accessed Mar. 31, 2020).

[58] LPKF, “Circuit Board Plotter ProtoMat S64.” https://www.lpkfusa.com/products/pcb_prototyping/machines/protomat_s64/ (accessed Jun. 13, 2020).

VITA

Waleed Al-Shaikhli was born in Baghdad, Iraq, where he attended Al Mutamaizen High School. He arrived in Kansas City as a refugee in 2008, where he graduated from Sumner Academy of Arts & Science. After high school, he attended area community colleges and transferred to the University of Missouri-Kansas City, where he received a bachelor's degree in Electrical and Computer Engineering then continued graduate school. In 2014 he started a small retail business with his brother, and in 2016 he founded the KC Muslim Civic Initiative a civil rights nonprofit based in Kansas City. During college, he held internships at the National Institute of Standards and Technology in Boulder, CO, and Honeywell Federal Manufacturing and Technology in Kansas City, MO. Post-graduation he plans to join the Global Security RF team at Honeywell Federal Manufacturing and Technology.